The stratigraphic record and processes of turbidity current transformation across deep-marine lobes — Source link ⧉

Ian A. Kane, Anna Pontén, Brita Vangdal, Joris T. Eggenhuisen ...+3 more authors

Institutions: Equinor, Utrecht University, University of Leeds

Related papers:

- Hybrid sediment gravity flow deposits – Classification, origin and significance

- Evolution, architecture and hierarchy of distributary deep-water deposits: a high-resolution outcrop investigation from the Permian Karoo Basin, South Africa

- Frontal and lateral submarine lobe fringes: Comparing sedimentary facies, architecture and flow processes

- "Linked" debrites in sand-rich turbidite systems - origin and significance

- Subaqueous sediment density flows: Depositional processes and deposit types

eprints@whiterose.ac.uk
https://eprints.whiterose.ac.uk/

1
2
3
4
5
6
7
8
9
10
11
12
13
14
15
16
17
18
19
20
21
22
23
24
25
26
27
28
29
30
31
32
33
34
35
36
37
38
39
40
41
42
43
44
45
46
47
48
49
50
51
52
53
54
55
56
57
58
59
60

1   **The stratigraphic record and processes of turbidity current transformation across deep-**

2   **marine lobes**

3

4   Ian Kane[1*], Anna Pontén[2], Brita Vangdal[3], Joris Eggenhuisen[4], David M. Hodgson[5], Yvonne T.

5   Spychala[5,4]

6   [1]*Statoil ASA, Exploration, NO-1364, Oslo, Norway*

7   [2]*Statoil ASA, Research Centre Rotvoll, NO-7005 Trondheim, Norway*

8   [3]*Statoil ASA, Research Centre Bergen, NO-5020, Bergen, Norway*

9   [4]*Faculty of Geosciences, Utrecht University, PO Box 80021, 3508TA Utrecht, The Netherlands*

10   [5]*School of Earth and Environment, University of Leeds, LS2 9JT, United Kingdom*

11   **Present address: School of Earth, Atmospheric and Environmental Sciences, University of*

12   *Manchester, Oxford Road, Manchester M13 9PL, United Kingdom*

13   **Abstract**

14   Sedimentary facies in the distal parts of deep-marine lobes can diverge significantly from those

15   predicted by classical turbidite models, and sedimentological processes in these environments are

16   poorly understood. This gap may be bridged using outcrop studies and theoretical models. In the

17   Skoorsteenberg Fm., a downstream transition from thickly-bedded turbidite sandstones to

18   argillaceous, internally layered hybrid beds is observed. The hybrid beds have a characteristic

19   stratigraphic and spatial distribution, being associated with bed successions which generally coarsen-

20   and thicken-upwards reflecting deposition on the fringes of lobes in a dominantly progradational

21   system. Using a detailed characterisation of bed types, including grain size, grain fabric and

22   mineralogical analyses, a process-model for flow evolution is developed. This is explored using a

23   numerical suspension capacity model for radially spreading and decelerating turbidity currents. The

24   new model shows how decelerating sediment suspensions can reach a critical suspension capacity

25   threshold beyond which grains are not supported by fluid turbulence. Sand and silt particles, settling

26   together with flocculated clay, may form low yield-strength cohesive flows; development of these

27   higher concentration lower boundary layer flows inhibits transfer of turbulent kinetic energy into the

28   upper parts of the flow ultimately resulting in catastrophic loss of turbulence and collapse of the

29   upper part of the flow. Advection distances of the now transitional to laminar flow are relatively

30   long (several km) suggesting relatively slow dewatering (several hours) of the low yield strength

31 flows. The catastrophic loss of turbulence accounts for the presence of such beds in other fine-

32 grained systems without invoking external controls or large-scale flow partitioning, and also

33 explains the abrupt pinch-out of all divisions of these sandstones. Estimation of the point of flow

34 transformation is a useful tool in the prediction of heterogeneity distribution in subsurface systems.

35 *Keywords: Hybrid beds, transitional flow deposits, flow transformation, deep-marine channels and*

36 *lobes, reservoir quality, flow capacity, Karoo*

37

Introduction

39 Observation and interpretation of sedimentary facies from deep-marine lobe deposits has been

40 strongly influenced by models developed from relatively small and coarse-grained basins, for

41 example the Annot sub-basins (Bouma, 1962) and the Californian Borderlands (Lowe, 1982).

42 However, today's ultra-deep-water subsurface exploration targets are typically associated with

43 sedimentary systems that are up to orders of magnitude larger, drained much larger areas, and are

44 significantly finer grained (e.g. the Wilcox Fm. of the Gulf of Mexico, Zarra et al., 2007). The

45 sedimentary environments and facies distributions of these systems are understudied as they

46 commonly develop on passive margins and may overlie transitional or oceanic crust, and as such are

47 prone to subduction. Numerous studies have documented these systems from remote sensing-based

48 observations and slightly more limited core data from the modern and Holocene stratigraphy (an

49 excellent example being the Mississippi Fan, see summary in Twichell et al., 2009). Due to the

50 paucity of outcrops revealing such systems, it may be appropriate to use fine-grained systems in

51 smaller basins as process analogues to larger systems (e.g. Martinsen et al., 2000; Sullivan et al.,

52 2000). In these fine-grained systems, complicated facies and facies distributions, which diverge

53 significantly from classical turbidite models, are reported from medial and distal lobe settings

54 (Haughton et al., 2003, 2009; Sylvester & Lowe, 2004; Talling et al., 2004, 2012; Amy & Talling,

55 2006; Ito, 2008; Barker et al., 2008; Davies et al., 2009; Hodgson, 2009; Kane & Pontén, 2012;

56 Pyles & Jennette, 2012; Talling, 2013; Grundvåg et al., 2014; Terlaky & Arnott, 2014; Fonnesu et

57 al., 2015; Southern et al., 2015, 2016; Spychala et al., in revision). Such beds have been termed

58 hybrid event beds by Haughton et al. (2009), which emphasises that an individual bed represents the

59 deposits of different types of flow within the same event. Typically, this is a basal turbidite and an

60 upper debrite; the term has, however, been adopted to cover a wide range of deposit and process

61 types which combine to form a single 'hybrid' bed (e.g., Hodgson, 2009; Talling, 2013; Fonnesu et

62 al., 2015). The stratigraphic and spatial complexity of these bed types means that deep-marine fan

63 systems represent significant challenges for reservoir prediction at both exploration and development

64 scales (Porten et al., in press). The Paleogene Wilcox Fm. exemplifies these challenges: it is

65 characterised by extremely large volumes of sandstone, but often occurring as mud-rich sandstones

66 with marginal reservoir quality (i.e., low porosity and permeability values), with stratigraphically

67 and spatially isolated higher-quality reservoir sandstones (Zarra, 2007; Kane and Pontén, 2012).

68 In this contribution, the spatial and stratigraphic distribution of the various sedimentary facies

69 associated with proximal, medial and distal deep-marine lobe environments of Fan 3,

70 Skoorsteenberg Fm., Tanqua Karoo, are presented and characterised, with particular emphasis on

71 hybrid beds. The paper comprises two interlinked sections, with the main focus being 1) to

72 characterise fine-grained hybrid beds, and 2) to develop a process based numerical model for their

73 observed occurrence. In the first part, we use outcrop and petrological observations to infer

74 sedimentological flow processes. In the second part, a numerical model is introduced to investigate

75 the inferred processes. The model uses a suspension-capacity model (Eggenhuisen et al., 2016), and

76 applies it to radially spreading decelerating flows. Integrating the detailed bed characterisation and

77 the numerical model, we propose that these types of hybrid beds form due to the loss of turbulence

78 due to flow deceleration, the development of internal stratification and eventual catastrophic loss of

79 turbulence in the flow. Understanding of the process sedimentology of these deposits and their

80 stratigraphic and spatial distribution can be applied to systems of similar grain-size range to

81 significantly reduce subsurface uncertainty and to improve prediction.

82

83 **Data and Methods**

84 The dataset comprises 20 sedimentological logs collected in the field and correlated by walking out

85 individual beds (Fig. 1). These logs were collected at 1:20 scale with more detailed logs of

86 individual beds and packages of beds collected at 1:2 scale (Figs. 2-5). Aerial photographs supported

87 field correlation in areas that were difficult to access or were covered (Fig. 2). Data collected

88 include lithology, bed thickness, and palaeocurrent measurements from ripples, flutes and other sole

89 marks. In addition, the equivalent stratigraphic intervals within cores from 7 research boreholes were

90 logged at 1:20 scale (Fig. 3).

91   Petrographic analysis was performed from 49 orientated thin sections. Although not strongly

92   cemented, point-counting is challenging due to the high degree of compaction and commonly large

93   proportion of clay. For this reason, further analytical work using the QEMSCAN® (Quantitative

94   Evaluation of Minerals by SCANning electron microscopy) was undertaken on 39 samples to

95   quantitatively analyse the mineralogy and texture of different bed types in order to support

96   qualitative outcrop observations. QEMSCAN® uses an FEI Quanta 650F SEM (Scanning Electron

97   Microscope) with two silicon drift energy-dispersive X-ray spectrometers (Pirrie et al., 2004). X-ray

98   and backscattered electron signals are used to image and create quantified mineralogical maps of

99   thin sections with a resolution of 5 μm). Typically, framework mineral grains are isolated within, or

100 coated by, the clay matrix and they can be imaged separately by the QEMSCAN®. These grains can

101 be measured and grain size distributions made from the resultant large datasets (1×10^5 - 2×10^6 grains

102 per section). Grain size is determined according to the long axis, which is automatically measured in

103 thin section. As with traditional thin-section point-counting, this method underestimates grain-size

104 diameter by 11%, or by 0.2 phi units (Johnson, 1994). The smallest grains measured are 5 μm, which

105 does not significantly truncate the fine tail end of the grain size spectrum.

106

107 **Geological setting of the Karoo Basin, Tanqua Depocentre and Skoorsteenberg Fm.**

108

109 During the Permian, the Karoo Basin is interpreted as either a retro-arc foreland basin developed

110 inboard of a fold and thrust belt (De Wit and Ransome, 1992; Veevers et al., 1994; Visser and

111 Prackelt, 1996; Visser, 1997; López-Gamundí and Rossello, 1998), or, to subsidence caused by

112 dynamic topography related to subduction (Pysklywec and Mitrovica, 1999; Tankard et al., 2009).

113 The Tanqua depocentre (Fig. 1A) was a topographic 'low' developed within the south-western part

114 of the Karoo Basin, and is bound by an oroclinal bend in the Cape Fold Belt, with the Cederberg

115 branch bounding the western margin and the Swartberg Branch bounding the southern margin. The

116 depocentre is filled by sediments of Westphalian (Carboniferous) to Triassic age, which comprise

117 the Karoo Supergroup. These sediments record the late Palaeozoic deepening and then shallowing of

118 the basin (Hodgson, 2009). The Karoo Supergroup is subdivided into the glaciogenic Dwyka Group

119 (Westphalian to early Permian), the marine Ecca Group (Permian) (Fig. 1C) and the non-marine

120 Beaufort Group (Permo-Triassic) (Smith, 1990).

121   In the Tanqua depocentre, the Ecca Group comprises an approximately 1400 m thick

122 succession of siliciclastic sediments (Wickens, 1994; King et al., 2009). The lower Ecca Group (the

123   Prince Albert, Whitehill, and Collingham formations) is overlain by >600 m of mudstone and

124   siltstone (Tierberg Fm.; Hodgson et al., 2006), which in turn is overlain by a c.400 m thick fine-

125   grained interval of sand-rich submarine fans, separated by extensive claystone and siltstone intervals,

126   forming the progradational Skoorsteenberg Fm. (Wickens, 1994; Morris et al., 2000; Johnson et al.,

127   2001; Wild et al., 2005; Hodgson et al., 2006, Hodgson 2009; Prélat et al., 2009; Spychala et al., in

128   revision) (Fig. 1). The Kookfontein Fm. overlies the Skoorsteenberg Fm. and is a c.300 m thick

129   succession representing a submarine slope and shelf-edge delta, shallowing-up to deltaic and

130   shoreface deposits (Wild et al., 2009; Poyatos-More et al., 2016).

131

132   *Skoorsteenberg Fm.*

133   The c. 400 m thick Skoorsteenberg Fm. consists of five fine-grained sandy intervals, interpreted as

134   four submarine fans (Fans 1-4) and an overlying base-of-slope to lower slope succession termed Unit

135   5 (Bouma & Wickens, 1991; Wickens, 1994; Morris et al., 2000; Johnson et al., 2001; Wild et al.,

136   2005; Hodgson et al., 2006) (Fig. 1). To retain consistency with previous literature, the 'fan'

137   nomenclature is retained, which has been used as a lithostratigraphic term and encompasses a linked

138   system of sandstone and siltstone channel-fills and lobe bodies. Collectively, the lobes of Fan 3 may

139   be regarded as a lobe-complex set (c.f. Prélat et al., 2009). A robust stratigraphic framework for the

140   formation has been established by several field studies (Wickens and Bouma, 1991; Wickens, 1994;

141   Bouma and Wickens, 2001; Johnson et al., 2001; Hodgson et al., 2006; Hodgson, 2009; Prélat et al.,

142   2009; Hofstra et al., 2015). This has been augmented by seven research boreholes and together this

143   has allowed the development of a detailed evolutionary model for the fan intervals (Hodgson et al.,

144   2006; Luthi et al., 2006). Fan 3 is interpreted to record a pattern of initiation, followed by

145   progradation and aggradation, to retrogradation (Hodgson et al., 2006). Within a sequence

146   stratigraphic framework, each fan has been interpreted to represent a lowstand systems tract and the

147   overlying regional claystone and siltstone as the combined transgressive and highstand systems tract

148   (Goldhammer et al., 2000; Johnson et al., 2001; Hodgson et al., 2006). The chronostratigraphic

149   framework for the fans remains poorly constrained, although recently published U–Pb single-grain

150   zircon ages from volcanic ash layers indicate an overall late Permian age (c.255 Ma, Fildani et al.,

151   2007, 2009; McKay et al., 2015).

152   Lithofacies of the submarine fans have been described previously (Morris et al., 2000;

153   Sullivan et al., 2000; Johnson et al., 2001; van der Werff and Johnson, 2003a, 2003b; Hodgson et al.,

154   2006; Hodgson, 2009; Prélat et al., 2009; Groenenberg et al., 2010; Jobe et al., 2012; Hofstra et al.,

155   2015). This study focuses on hybrid beds within Fan 3, which have been described previously as bi-

156   and tri-partite turbidites with slurry or debris flow caps (Morris et al., 2000; Johnson et al., 2001;

157   Hodgson et al., 2006; Luthi et al., 2006). Hodgson (2009) expanded on this work and interpreted

158   these beds as 'hybrid beds' (equivalent to 'hybrid event beds' *sensu* Haughton et al., 2009). Hodgson

159   (2009) interpreted the upper parts of these composite beds as 1) the deposits of debris-flows derived

160   from partial flow transformation after shelf-edge collapse; 2) developed through flow transformation

161   from turbidity currents entraining a muddy substrate; or 3) representing the mudstone clast-rich tails

162   of turbidity currents where the matrix was not argillaceous. Johnson et al. (2001) and Hodgson et al.

163   (2009) noted a preferential geographic distribution of these beds at the fringes of lobe deposits, with

164   Hodgson (2009) attributing a preferential stratigraphic distribution at the base of lobe complexes to

165   slope incision during fan initiation and progradation phases.

166

167   **Results**

168   **Lithofacies**

169   The lithofacies presented here represent 'event beds' and are classified based on outcrop

170   observations (Figs. 2-7) following the approach of Johnson et al. (2001), Hodgson et al. (2006) and

171   Hodgson (2009), utilising the latter's four-fold lithofacies scheme, which is particularly relevant to

172   the fringe facies of lobes. The detailed characterisation of samples from individual beds, presented

173   below is used to support the necessary degree of interpretation of features from outcrop, e.g., mud

174   content (n.b. 'mud' is used here as a general term for mixtures of clay, silt, organic fragments and

175   clay flocs and clasts). Nevertheless, outcrop-based observations/interpretations of relative clay-

176   content closely match quantitative data from analytical techniques, giving confidence in this

177   approach. Therefore, the analysis below is based on outcrop and core observations and provides a

178   framework for the more detailed analyses that follow.

179   *Thick-bedded sandstones (0.6-6 m)*

180   Thick-bedded sandstones are very-fine to fine-grained, generally lacking primary structures but may

181   be marked by dewatering structures, predominantly pillars and lesser dishes; these are subtle features

182   at outcrop and are more clearly visible in core (Fig. 8H). These 'beds' are often amalgams of several

183   beds (e.g., capping Lobe 5, Fig. 2A and C; and Log SK3, Fig. 4). Bed amalgamation can be

184   enigmatic in outcrop, but is more readily observed in core, where typical features comprise

185   mudstone rip-up clasts, subtle grain size changes and truncated dewatering structures. Rarely, bed

186   tops preserve some tractional structures, plane parallel-lamination and ripple cross-lamination, in

187   conjunction with a normal grading profile. Bed bases are sharp, and commonly truncate underlying

188   beds in angular steps (Fig. 6B). Flutes and tool marks are present, but not common. It is less

189   common to see loading at the bases of these thick beds than the thinner-bedded sandstones.

190   Interpretation: Characteristic features of turbulent flow, such as flutes, tools, normal grading and

191   tractional structures suggest that these beds are turbidites. The general lack of structure throughout

192   most of these beds might in part reflect the often pervasive dewatering, which is apparent in core,

193   but generally not at outcrop. Hodgson (2009) suggests that the overall fine grain size, and its narrow

194   range, preclude the interpretation of flow concentration and sub-division into low-, medium- or high-

195   density turbidites, although tractional structures are generally well developed in many of the thinner

196   turbidites. Based on the observations above and the further discussion of mineralogical and textural

197   data presented below, these deposits are interpreted for the most part as high-density turbidites,

198   *sensu* Lowe (1982).

199   *Thin-to-medium bedded sandstones (0.1-0.6 m)*

200   Very-fine to fine-grained sandstones are generally normally-graded and dominated by tractional

201   structures (ripple- and plane-parallel lamination) (e.g., see Log SK5, interval 7-9 m); in outcrop

202   tractional structures can be very subtle (Fig. 8A). The lower parts of beds may be structureless. Bed

203   bases are sharp, flat lying, and may be marked by flute casts, whilst bed tops may contain abundant

204   organic material and mudstone clasts in a clean sand matrix, and may preserve ripple forms. Banding

205   occurs in some parts of the fan, but can be difficult to discern in the field, being clearer in core (Fig.

206   8F).

207   Interpretation: Based on their tractional structuration, normal grading and flute casts, beds of this

208   lithofacies are interpreted as low- to medium-density turbidites deposited by low- to medium-

209   concentration turbidity currents (*sensu* Lowe, 1982). Banding may reflect some periodic suppression

210   of turbulence associated with flow deceleration or increased concentration (Lowe & Guy, 2000;

211   Barker et al., 2008).

212   *Siltstones and thin-bedded sandstones (individual beds <0.1 m)*

213   This lithofacies comprises siltstone to very-fine grained sandstone beds that are commonly

214   interbedded (e.g., interval 1.5-2.5 m, Log Sk20, Fig. 4; Fig. 7). These are typically normally-graded,

215   plane-parallel laminated and/or ripple cross-laminated and sometimes have small flute and tool

216 marks on their bases. In the distal parts of lobes (Prelat et al., 2009) climbing ripple lamination,

217 common in proximal areas, is not observed.

218 Interpretation: Their tractional structuration and normal grading leads to an interpretation of these

219 beds as turbidites deposited by low-density turbidity currents (*sensu* Lowe, 1982).

Hybrid beds

221 The focus of this study is the character and prevalence of hybrid beds in frontal lobe fringe deposits

222 (sensu Spychala et al. in revision). Frontal fringe here denotes the distal and frontal part of the lobes,

223 approximately 5 km from their pinch-out, following and consistent with Hodgson (2009) and Prélat

224 and Hodgson (2013), and approximately 25-30 km downdip from the channelized to unconfined

225 areas. In contrast, lateral lobe fringes have rare hybrid beds and are dominated by low-density

226 traction-dominated turbidites (Spychala et al. 2016; in revision).There is a wide range of lithofacies

227 within the hybrid-bed class, and these can be laterally variable within individual beds over the scale

228 of tens of centimetres (Fig. 7). There is a general down-flow progression from deposits that appear

229 more turbiditic to deposits with the character of debrites.

230

Thick-bedded hybrid beds (0.6-1.2 m)

232 These occur approximately 5 km from pinch-out. Commonly, thick (up to 1.2 m) beds with stepwise

233 basal erosional cuts (cm-decimetre scale) into the substrate that lack loading and other soft-sediment

234 deformational structures (e.g., bed at 5.4 m SK5, Fig. 4). Beds are generally graded throughout with

235 upper parts that are slightly more clay rich (c. 5-10%, see mineralogy section) and commonly clast

236 rich. These are similar to the thick-bedded turbidites described above but form part of a continuum

237 with the deposits described below, characterised by increasing mud content at bed tops.

Interpretation

239 In the channel-fills and scour-fills at and beyond the channel-lobe transition (e.g., Hofstra et al.,

240 2015), erosion and entrainment of the weakly consolidated substrate resulted in sharp basal surfaces

241 to turbidites, and the incorporation of intrabasinal clasts. This erosional behaviour seems to have

242 persisted across much of the proximal and medial part of the lobes, at least associated with the larger

243 events, to these relatively distal positions. Entrained substrate was rapidly broken up within the flow

244 often resulting in clast and clay-rich divisions at bed tops. The absence of soft-sediment deformation

245 structures in the underlying substrate is interpreted to be due to excavation of the soft substrate to a

246   firm layer where the substrate shear strength is greater than that of the shear stress exerted by the

247   overriding flow.

248

Thin- to medium-bedded hybrid beds (0.1-0.6 m)

250   These occur approximately 3 km from pinch-out. Beds in this 'position' are complicated, with

251   intensely loaded bases and flame structures. Beds are a few to 60 cm thick, but pinch and swell as

252   they load into underlying substrate (e.g., bed at 1-2.5 m Log SK1, Fig. 4; 0-1 m Log SK4, Fig. 5;

253   Figs. 7A, 8). Locally, sections of substrate are fully or partially lifted into the bed. A patchy

254   development of internal layering is observed, with cleaner lower sandstone divisions (c. 10-15%

255   clay, see mineralogy section below), and muddier upper sandstone divisions (c. 30-35% clay) that

256   appear intermittently laterally and extend for 10's to 100's of cm. Rare thin silty caps are observed.

257

Interpretation

259   The description demonstrates interaction of an overriding flow with the substrate that, owing to the

260   lower energy of the flows compared to proximal areas, leaves a record of partial or incomplete

261   substrate entrainment. The development of internal layering and the lateral variability suggests that

262   flows increased in concentration but had not developed stable density stratification. The general lack

263   of a silty cap to these beds suggests that the material was mixed within the argillaceous upper parts

264   of these beds and that the flows were undergoing transformation.

265

Thin-bedded hybrid beds (<0.1 m)

267   These occur predominantly <1 km from pinch-out. Typically, bi- or tri-partite beds, although some

268   beds have four internal divisions (Figs. 7 & 8). From the base these divisions are: 1) a very-fine-

269   grained sandstone, which is relatively mud-poor with respect to the upper divisions, and always

270   lacking macroscopic tractional structuration. The boundary with the overlying division is typically

271   sharp and may be marked by bed-parallel mudstone clasts; 2) an argillaceous sandstone with a bed-

272   parallel or inclined shear fabric (Fig. 7); 3) a highly argillaceous sandstone with high organic

273   fragment content and a strongly sheared fabric; 4) rare examples have a siltstone cap. Additional

274   internal divisions of variable mud content are common and these typically have the characteristic

275   sheared appearance noted above. In outcrop, mud content is qualitatively determined by colour and

276   weathering style, with muddier beds typically having a more 'bulbous' nature or spherical

277   weathering pattern typical of homogenous rocks. Bed bases are flat to slightly undulose in distal

278   localities, sometimes slightly loaded with rare, small (mm-scale) flame structures.

279

280   *Interpretation*

281   The high mud content of these deposits suggests deposition from higher concentration flows than

282   their up-dip equivalents, which were depositing en-masse and potentially behaving as transitional to

283   laminar flows. The strong internal layering of these deposits is interpreted to reflect the development

284   of discrete rheological zones within the flow in response to radial spreading of flows, deceleration,

285   and increase in near bed flow concentration. The lowermost sand layer shows no evidence for

286   deposition by turbulent flow, being devoid of erosional or tractional structures with the exception of

287   rare grooves or tool marks, and has a high matrix content (see mineralogy section). Instead, the

288   sandier part of the bed is interpreted to represent the deposit of a high-concentration flow where

289   yield strength was the principal particle support mechanism. The basal layer is typically relatively

290   cleaner than the overlying layer(s) which may reflect the ability of the coarser particles in the flow to

291   settle to its base, suggesting the flow had relatively low strength (e.g., Sumner et al., 2009; Talling,

292   2013). Clasts along the intra-bed boundaries may represent kinetic sieving, with the larger clasts

293   working their way to the top of the lowermost bed division due to grain collisions in the low strength

294   transitional to laminar flows; alternatively, as grain collisions become less important (i.e., at higher

295   concentrations) buoyancy may have become more important. Upper bed divisions are interpreted to

296   be debris-flow deposits, based on their poor sorting and high matrix content (see *Mineralogy* section

297   below), suggesting a complete flow transformation took place. These divisions are interpreted to

298   reflect, in part, a longitudinal flow structure, rather than representing the one-to-one vertical

299   structure of the flow.

300

301   ***Mineralogy***

302   Results:

303   Chemical and petrological analysis of thin sections has allowed the mineral composition of the

304   different facies types to be determined (Figs. 9-12). On a quartz-feldspar-lithic ternary diagram the

305   samples plot as lithic arkoses and feldspathic litharenites. An outcrop subdivision of samples into

306   'turbidites' and 'hybrid beds' shows that turbidites fall entirely within the lithic arkose class, whilst

307   hybrid beds span the lithic arkose and feldspathic litharenite classes (Fig. 9). The wide range of

308   mineral types identified (Table 1 and Figs. 10 & 11) have been grouped together, for the purpose of

309   examining bed-scale mineralogical variability, into the following three classes, which together form

310   >90% of each sample: 1) quartz, 2) feldspar, and 3) clay. Of the clays, illite is most abundant; from

311   petrological analysis this appears to be primarily detrital in origin, although it could have been

312   altered from another detrital clay form, most-likely smectite or kaolinite; in either case it does not

313   appear to be a diagenetic mineral. In addition to detrital illite (or clay in general), there could be a

314   much smaller contribution from alteration of muscovite or feldspar (Fig. 12). The analysis reveals

315   distinctive mineralogical trends for the hybrid beds and turbidites (Fig. 13). Quartz is the dominant

316   detrital mineral, with slightly lower proportions of feldspar. Muscovite mica represents only 1-2% of

317   the mineral volume with no significant variability between hybrid beds or turbidites (Table 1).

318   Overall quartz is more abundant by proportion in the turbidites than in the hybrid beds, whereas

319   feldspar content remains approximately the same in both bed types (e.g., samples F and G; Fig. 13).

320   Clay content increases from bed bases to bed tops, with values in the lower parts of hybrid beds in

321   the range of 20-25%, compared to around 10% at the base of turbidites; this rises to 25-35% and 20-

322   25% respectively (Fig. 13).

323   Interpretation:

324   Compositional differences between hybrid beds and turbidites show a higher lithic content in the

325   former, which partly reflects the higher proportion of mudstone and siltstone clasts incorporated

326   within the hybrid beds. There is no significant difference in the heavy mineral distribution,

327   suggesting that flows across the lobes had a common source. The confirmation of higher mud

328   content in argillaceous divisions of hybrid beds validates the qualitative interpretations of mud

329   content based solely on outcrop observations presented both above and in Hodgson (2009). The

330   apparent strong internal layering of the hybrid beds observed at outcrop is clearly demonstrated to be

331   directly linked to mud content that gives good confidence in the interpretation of graphic logs

332   collected during this study. The relatively low clay content of turbidite sands is expected and has

333   been documented in other studies, e.g., Sylvester & Lowe (2004), and is accounted for by the fine

334   sediment being maintained in suspension as the coarser grains settle out.

335   ***Grain size***

336   *Results:*

337   Grain size was determined using QEMSCAN[®]. Individual framework grain outlines (quartz and

338   feldspar) were extracted from the matrix material, to provide an overview of the 5-500 μm grain-size

339   spectrum. Grain size is illustrated as simple plots of trends within individual beds (Fig. 13), and as

340   entire grain-size distributions (Fig. 14). Peaks in the range of 200-500 μm are generally either

341   amorphous clay bodies or claystone clasts, and some minor cemented quartz grains. The grain-size

342   distribution curves illustrate the 'skew' of the grain size population, which can be described as

343   positively skewed when the sample has excess fine grained material (fine skewed), symmetrical,

344   when the distribution is even, or negatively skewed when the sample has an excess of coarse

345   material (e.g., Moiola and Weiser, 1968). In broad terms, turbidites have lower and middle divisions

346   characterised by positively skewed distributions, to symmetrical distributions in their upper

347   divisions, whereas hybrid beds are characterised by negatively skewed lower and middle divisions,

348   shifting to more symmetrical distributions in their upper parts (Fig. 15).

349   *Interpretation:*

350   The mean and maximum grain size of quartz and feldspar in turbidites is generally larger than in the

351   hybrid beds, suggesting that flow transformation took place sometime after the larger grains had

352   settled from suspension in turbulent flows. Typically, en-masse sedimentation would give a broad

353   positively skewed distribution, whilst a winnowed deposit, such as a beach sand, would be coarsely

354   skewed (Moiola and Weiser, 1968). The turbidites show a fine skew, indicating sedimentation of the

355   entire grain-size spectrum with minimal reworking, whereas the hybrid beds are coarsely skewed,

356   indicating that they have an excess of coarse grains in them. An explanation for this is that the

357   coarser grains were able to settle through a low yield strength muddy flow, akin to the late stage

358   settling described experimentally by Sumner et al. (2009). The upper parts of these beds, interpreted

359   as the deposits of higher yield strength flows to fully laminar flows, are characterised by

360   symmetrical distributions reflecting the full grain size distribution available during flow and

361   deposition.

362

363   *Fabric analysis*

364   Grain orientation is constrained using the least-projection method, which is defined as the direction

365   of the two most-closely spaced parallel lines that can be drawn tangentially to the edges of the

366   longest section of a grain (Dapples and Rominger 1945; Baas et al. 2007). Grain-fabric analysis

367   allows inferences of flow conditions to be made where macroscopic structures are not present.

368   Alignment of long axes occurs in most depositional regimes (although not all, see review by Baas et

369 al. 2007). The samples are devoid of macroscopic tractional structuration meaning that problems

370 regarding the orientation of long-axes with regards to palaeoflow, such as the presence of flow-

371 oblique fabrics or flow-transverse fabrics (typical of ripple cross-lamination), are avoided (see

372 Hiscott & Middleton 1980; Baas et al. 2007, and references therein). The purpose of the analysis is

373 to compare relative grain-fabric differences between bed divisions in individual beds, as this may

374 yield information about the depositional conditions and syn-depositional shearing of the bed. It is

375 stressed that although the sample orientation is consistent for individual beds (parallel to bedding),

376 the orientation with respect to palaeoflow is constrained only by the overall orientation of Fan 3 (e.g.

377 Hodgson et al. 2006; Luthi et al. 2006; Prélat et al. 2009). Grain alignment is influenced by section

378 orientation with respect to palaeoflow, which potentially differed between divisions in individual

379 beds. Nevertheless, the approach gives some support to observations and inferences made in the

380 field, and provides a relative comparison between bed divisions, which is the principal utility here.

381 Long axes were recorded using an automated QEMSCAN® process, meaning that a large number of

382 samples can be analysed quickly (1-2 orders of magnitude more grain measurements than typical

383 manual thin-section fabric studies, e.g., Kane et al., 2010a).

384 Results:

385 With one exception, samples from hybrid beds show Von Mises type distributions (normal circular

386 distribution) with vectorial concentrations (K, a measure of mean vector strength) in the range of

387 0.17-0.75, with a mean value of K = 0.5. In contrast, turbidites are characterised by Von Mises and

388 uniform distributions, distributions with low K values, from 0.04-0.6 with a mean value of K=0.26

389 (Table 2 and Fig. 13).

390 *Interpretation:*

391 Hybrid beds have a strong grain orientation in comparison to the turbidites (Fig. 13); this fabric is

392 attributed to shearing within the cohesive flow. The low K values for the turbidites support their

393 origin as deposits from high-density turbidity currents where sediment deposition to the bed

394 precluded significant bedload transport or grain organisation. Deposits of low-density turbidity

395 currents, reported in a previous study by Kane et al. (2010a), have better organisation than these

396 deposits with Von Mises and Gaussian (non-circular) distributions, illustrating grain organisation by

397 tractional processes. The strong fabric reported for these hybrid beds suggests that the high-

398 concentration flows, to which they are attributed, were still relatively fluidal with internal shear

399 layers along which elongate grains are aligned.

Stratigraphic and spatial distribution of bed types

400

401 Typically, the Fan 3 stratigraphic succession is marked at its base by silty low-density turbidites,

402 which progressively thicken and coarsen upwards from fine siltstones to very-fine sandstones (Figs.

403 4 & 5). In some places, the first medium to thick beds occur abruptly at the base of the sandy part of

404 Fan 3, and are then overlain by several variably well-developed thickening- and coarsening-upward

405 packages, which are interpreted to represent the individual lobe deposits (Fig. 2). Bed thickness

406 patterns are, however, variable (Prélat and Hodgson, 2013). Fine-scale mapping and correlation by

407 Prélat et al. (2009) led to extensive thin-bedded successions being treated as distinct elements, and

408 were interpreted as the distal fringes of lobes (Prélat and Hodgson, 2013), implying a pronounced

409 compensational stacking pattern. Hybrid beds are found within the lower to middle part of the Fan 3

410 succession in the distal areas, and are interbedded with turbidites. Within the turbidite succession

411 described above the hybrid beds stack from the distal-, to medial to proximal lobe fringe types

412 described above (Figs. 4 & 5). Interbedded throughout the succession are packages of thin-bedded

413 sandstone and siltstone low-density turbidites. High-density turbidites, and thick-bedded turbidites of

414 uncertain affinity, are well developed in the feeder channel-fills, axial and off-axis areas of the lobes,

415 down-dip of scours and in association with channelised features developed across the lobes; they

416 generally occur at the top of individual lobe stratigraphic units, but can occur at their bases (Morris

417 et al., 2000; Johnson et al., 2001; Hodgson et al., 2006).

Interpretation

418

419 The character of flows passing over the Fan 3 lobes can be subdivided into turbidity currents, which

420 deposited a range of low- to high-density turbidites, and the higher concentration transitional or

421 laminar flows inferred above, which deposited hybrid beds. Low-density turbidites are common

422 across all environments and tend to increase in proportion and thin towards the distal pinch-out (e.g.,

423 Morris et al., 2000). The low concentration and relatively low degree of density stratification of the

424 flows allowed them to traverse gentle gradient changes associated with depositional relief across the

425 lobes (Groenenberg et al., 2010). High-density turbidites and transitional to laminar facies were

426 deposited by high-concentration flows, and appear to have been strongly controlled by topography

427 related to previous deposits (Groenenberg et al., 2010). High-density turbidites are related to the

428 main feeder channels and low-relief distributary channels developed across the lobe (e.g., Morris et

429 al., 2000; Johnson et al., 2001; Hodgson et al., 2006), and may be the expression of the flows that cut

430 major scours in the channel lobe transition zone (e.g., Hofstra et al., 2015). The flows that deposited

431   these facies are thought to have been strongly density stratified; as such, individual large magnitude

432   flows were able to make their own pathway(s) following depositional topography of precursor lobe

433   deposits and developing 'finger-like' bodies across the lobe (Groenenberg et al., 2010). Simple

434   trends of bed thickening associated with lobe progradation, which might be expected in the simplest

435   case (e.g., Mutti and Sonnino, 1981), are obscured by the juxtaposition of thicker beds marking

436   either the onset of a new lobe (but not always), or occurring apparently randomly within an

437   otherwise thickening (or thinning) upwards trend. Nevertheless, the hybrid beds are for the most part

438   associated with medial and distal lobe frontal fringe environments (cf. Spychala et al., in revision),

439   and are developed down-dip of high-density turbidites. Stratigraphically, therefore, the hybrid beds

440   typically occur in the basal parts of lobe successions (Hodgson, 2009). In addition, they can occur in

441   packages representing only the distal fringe of a lobe, i.e., in areas where the sandier parts of the lobe

442   did not reach (e.g., Log Sk4, Fig. 5). The point where transformation occurs is the subject of the

443   following section.

444

445   **Discussion**

446   **Fan 3 turbidity currents and flow transformation**

447   Whilst much of the Fan 3 stratigraphy is dominated by turbidites, sedimentary facies tracts and

448   stratigraphic stacking suggest that some turbidity currents transformed to transitional or laminar

449   flows (e.g. McCave & Jones, 1988; see review by Talling, 2013). This interpretation is based on the

450   downstream facies transitions described above, whereby turbidites pass downstream into hybrid

451   beds. The ability of a turbidity current to maintain sediment in suspension is affected by lateral

452   spreading and associated deceleration; we postulate that this alone can force local flow

453   transformation, resulting in deposition of a hybrid bed in the distal parts of a lobe.

454

455   The analysis utilises the suspension capacity parameter Γ (Eggenhuisen et al., 2016), a measure of a

456   flow's ability to maintain sediment in suspension, in conjunction with a geometrical model of flow

457   expansion. A simple numerical model is developed to show how Γ evolves as a turbidity current

458   spreads laterally and decelerates across a lobe. In this discussion, a 'lobe' scale is used rather than a

459   'lobe element' as the latter are less well-constrained. The suspension capacity parameter Γ represents

460   a force balance between the downward gravity force, F_g, and upward directed turbulent forces(F_{turb})

461   that can be used to compare dynamic turbulence scales to gravitational scales acting near the base of

462   turbidity currents. F_g is the net force resulting from buoyancy and gravity acting on sediment grains

463   in suspension. The turbulent force scale F_{turb} is derived from universal scaling of turbulent

464   Reynolds-stress gradients in the region just above the bed where turbulent structures are generated

465   that export excess turbulent kinetic energy that cannot be dissipated in the boundary layer upward

466   into the flow (Pope, 2000). This region will be a few millimetres to centimetres thick in a typical

467   turbidity current. The suspension capacity parameter Γ is given by (see Eggenhuisen et al. [2016] for

468   a full derivation):

469

470   $$\Gamma = \frac{F_{turb}}{F_g} = \frac{u_*^3}{140 v g R C_b}$$ (*Equation 1*)

471

472   Where u_* is the shear velocity, v is the kinematic viscosity of water (1.002 10^{-6} m^2/s), g is the

473   constant of acceleration by gravity, C_b is volumetric sediment concentration near the bed, and

474   $R = (\rho_s - \rho_f)/\rho_f$ is the relative density of sediment where ρ_s and ρ_f are the particle and fluid

475   density respectively (2650 kg m^{-3} for quartz and 1020 kg m^{-3} for seawater) giving R = 1.6. The

476   numerical constant 140 derives from universal scales of vertical turbulence in boundary layer flow

477   (Eggenhuisen et al., 2016).

478   Near-bed turbulence dominates suspension when Γ >1, and the turbulent conditions could maintain

479   more sediment in suspension, such that, additional sediment can be entrained into the passing flow if

480   it is readily available at the bed. This condition is therefore termed under-saturated with respect to

481   the turbulent suspension capacity of the flow. At $\Gamma = 1$, turbulent forces near the bed are equal to the

482   gravitational pull on the suspended particle load. This force balance prevents average net vertical

483   acceleration of the sediment particles and the fluid between them, and the flow is in saturation

484   equilibrium with suspended sediment near the boundary; in this condition C_b can be seen as a

485   saturation concentration.

486   Gravity dominates suspension when $\Gamma < 1$ and the upward turbulent forces are smaller than

487   downward gravitational forces applied to the fluid by the particles, this prevents turbulent

488   accelerations and results in turbulence extinction. This condition is termed over-saturated with

489   suspended sediment because the flow does not have sufficient turbulent capacity to suspend all the

490   particles present near the bed. A recent breakthrough in DNS simulations of turbidity currents

491   (Cantero et al., 2009, 2011, 2012) demonstrates how turbulence production at the base of turbidity

492   currents is shut-down rapidly in over-saturated suspensions, leading to rapid laminarization

493   extending upwards in the flow. The result will be increasing sediment stratification towards the base

494   of flow as there is no mechanism to counter the gravitational settling of sediment. A key outcome of

495   the work by Cantero et al. (2009, 2011, 2012) and Eggenhuisen et al. (2016) is that extinction of

496   turbulence can occur at very low absolute concentrations of suspended sediment. The conventional

497   perception that turbulence suppression occurs at high sediment concentrations is only true in very

498   high energy flows. Low concentrations suffice to fully suppress turbulence generation in moderate or

499   gentle flow conditions. Occurrence of hindered settling at sufficiently high sediment concentrations

500   can slow down and delay sediment accumulation rates to the base of the flow, but cannot stop

501   sediment in a laminarized flow from settling completely.

502   Equation 1 is coupled to a model describing the structure of an oversaturated turbidity current

503   spreading over a lobe, after exiting a channel mouth to investigate the evolution of Γ in the spreading

504   flow. Estimation of the suspension capacity parameter depends on an estimation of the shear velocity

505   from the flow scales:

506    $u^* = \sqrt{gH\bar{C}RS}$ *(Equation 2)*

507   Where $\bar{C}$ is the depth averaged concentration, H is the flow thickness [m] (see discussion below),

508   and S is the tangent of the slope [-]. in the model output, the turbidity current exiting the channel is

509   followed while it spreads out over the lobe. The flow is considered uniform, and its bulk discharge is

510   conserved, such that the product of depth averaged flow velocity, flow thickness, and flow width W

511   is constant as the current travels in direction x along the lobe:

512                         $Q_b = H(x)\overline{U(x)}W(x) = constant$ *(Equation 3)*

513   A drag coefficient C^d is used to set a fixed ratio between the average velocity and shear velocity:

514         $C^d = U/u^*$ *(Equation4)*

515   The value of the drag coefficient C^d is set to 0.005 (following Parker et al., 1987). Essentially, this

516   model describes a depth averaged flow structure at different positions during passage over a lobe

517   assuming that friction always balances gravitational driving force. The different positions are linked

518   by the volumetric requirement that all discharge debauched from the input condition of the channel

519   mouth is spread equally over the lobe surface by lateral spreading, not by consideration of energy in

520   the form of momentum changes, potential energy losses, or variations in the budget of turbulent

521   kinematic energy. This analysis is thus cruder than depth averaged simulations that solve such

522   energy equations. The purposeful simplicity of this model makes the system easy to investigate and

523   robust to the interrogation of first order controls on the flow structure with distance.

524   The main simplifying assumptions on the behaviour of the turbidity current are: there is no erosion

525   or deposition as source or sink terms in Eq. 3 (constant discharge). Slope gradient is constant, not

526   some decreasing function S(x) of along-lobe distance x. The drag coefficient is constant in Eq. 4,

527   and does not change with changing friction against the ambient water. The flow spreads out equally

528   over the lobe surface, and does not focus in preferential flow pathways. The effect of these

529   simplifying assumptions will be discussed following the main result.

530   The discharge can be expressed purely as a function of the flow geometry by substituting Eq.4 and

531   Eq.2 into Eq.3:

532   $$Q_b = \frac{\sqrt{g\overline{C}RS}}{\sqrt{C_d}} H(x)^{1.5} W(x) \qquad\qquad\qquad \textit{(Equation 5)}$$

533   The geometries of the channel deposits in the proximal areas of Fan 3 are used to constrain the flow

534   dimensions that fed from channels onto the lobe surfaces. Channel depth (h) is used as a proxy for

535   flow thickness (H); in Fan 3, channel depths (in the proximal parts of the stratigraphy) are in the

536   range of 5-13 m (e.g. Sullivan et al. 2000, from the Ongeluks River outcrops). This approach

537   provides a minimum value for flow thickness (e.g., El-Gawad et al., 2012) as flows may be

538   significantly super-elevated above the channel depth (e.g., Piper & Normark, 1983, Mohrig &

539   Buttles, 2007, Kane et al., 2010b), however, it is assumed that the channel depth values are within

540   the same order of magnitude as the original flow thickness. In a series of physical experiments,

541   Mohrig & Buttles (2007) demonstrated that over-spilling (super-elevated) channelized turbidity

542   current thicknesses were typically in the range of h/H ≤ 1.3. The relationship of channel fill

543   thickness to instantaneous channel depth is also not straightforward, but if we assume a minimum

544   depth of 13 m (maximum channel fill thickness) then, if h/H ≤ 1.3, we have a minimum estimate of

545   H=17 m at the lobe apex (i.e., channel to lobe transition area), negating burial compaction effects.

546   Groenenberg et al. (2010) estimated a thickness of 4 m based on the height of depositional relief in

547   the medial to distal parts of the lobe. Lobe width (W=15 km) is used as a proxy for the maximum

548   flow width and lobe length is taken as 25 km (Prélat et al., 2009). The flow is assumed to spread

549   evenly over the full width of the surface of the lobe, and the width is set to increase linearly from the

550   width of the channel at the lobe apex (250 m) to the full lobe width at a distance similar to the lobe

551   length. The evolution of flow thickness, flow velocity, and shear velocity with distance along the

552   lobe can now be resolved using these assumptions (Fig.16). Flow thickness is equal to the estimate

553   from channel depth at the lobe apex (17 m) and decreases rapidly proximally from 0-5 km to about 4

554   m thick (corresponding approximately to the values estimated by Groenenberg et al. 2010 for the

555   medial–distal lobe), and more slowly to the lobe termination at 25 km. Flow velocity and shear

556   velocity show similar patterns (Fig. 16B). The evolution of the suspension capacity parameter, Γ,

557   goes through the threshold value of 1, at which point turbulence is supressed at 21km from the lobe

558   apex and 4 km from lobe pinch-out (Fig. 16C).

559

Discussion of the numerical model

561   The model demonstrates that a laterally spreading turbidity current, without entrainment of eroded

562   substrate material (or water), will decelerate, thin and lose its suspension capacity as the bed shear

563   velocity decreases. The model is necessarily simple as there are many poorly constrained parameters

564   and spatially variable feedbacks that may obscure the analysis of the first order parameters

565   governing suspension capacity. However, whilst inclusion of such second order effects in the

566   equations presented would modify the predicted flow conditions for the estimated values of slope

567   and channel mouth concentration, and thereby the loci of the flow transformation, the first order

568   result that flow spreading can result in flow transformation in the distal sections of lobes remains.

569   Previous models have suggested flow collapse in a similar manner, but are reliant on the poorly

570   constrained gradient Richardson number (e.g. McCave and Jones, 1988) or the shear Richardson and

571   shear Reynolds numbers (e.g., Cantero et al., 2012). These approaches necessitate the incorporation

572   of grain-size and settling velocity to establish vertical gradients of velocity and concentration, and

573   are dependent on bulk-flow Reynolds numbers. The present model avoids these ambiguities.

574   The model presented above infers a homogenous and steady longitudinal flow structure, but it can be

575   envisaged that Γ varies spatially within the flow, as well as temporally as demonstrated. This is a

576   necessary simplification for the purposes of this discussion. The overall lobe body is by definition a

577   depositional unit; if the suspension capacity parameter sets deposition this would imply that $\Gamma = 1$ is

578   at the lobe apex/channel mouth. This may be explained by the longitudinal structure of the flows,

579   and the general trend of progradation through time, such that successive flows tend to step farther

580   basin-ward during the growth phase; this may include the precise position of the channel-lobe

581   transition and lobe apex (e.g., Hodgson et al., 2016; de Leeuw et al., 2016).

582   The longitudinal structure of the flows in terms of Γ may be expressed by the vertical facies

583   stacks in individual lobes. In proximal areas erosion surfaces overlain by relatively clean basal

584   sandstones may indicate that $\Gamma > 1$ during the passage of the head and body, switching to $\Gamma \leq 1$ during

585   deposition of the tail-end of the flow. Distally, muddy sandstones overly conformable bed bases,

586   have a high matrix content and display sheared fabrics, suggesting that basal flow was laminar from

587   the onset at its arrival at distal locations, i.e., $\Gamma < 1$.

588   The implication of the observed erosion in the proximal lobes suggests that flows exiting the

589   channel mouth were under-saturated ($\Gamma > 1$) but may also be diagnostic of bathymetric control on

590   flow behaviour at the confined-to- unconfined transition, e.g., a hydraulic jump. The purposeful

591   simplicity of the model has the benefit that the effects of the main simplifications can be isolated and

592   analysed.

593   *Erosion and deposition.*

594   The outcrops show evidence for erosion in proximal lobe locations, indicating that material was

595   entrained in the first few to 10 km after a flow exited the channel. Erosion would increase flow

596   volume, concentration and/or thickness, flow velocity, and bed-shear velocity in the proximal

597   section of the lobe to values exceeding those of the scenarios presented in Figures 17 and 18, and

598   thereby delay flow transformation. Deposition of sediment from the laminarised base of the flow

599   down-dip of flow transformation will decrease the amount of sediment in suspension, and thereby

600   bed shear stress, leading to inevitable collapse of the flow. Thus, erosion then deposition can cause

601   the flow transformation point to be located in more distal positions than those indicated by Figures

602   17 and 18, but would not alter the result that flow spreading is sufficient to force transition to

603   deposition from laminarised flow.

604   *Constant slope.*

605   Slope gradient is a main control on sediment bypass (Stevenson et al., 2015), and bypass-dominated

606   channels tend to form on gradients that are relatively steeper, whilst deposition-dominated lobes tend

607   to form on slopes that are relatively more gentle (e.g., Kneller, 2003). This decrease in slope is not

608   incorporated into the analysis presented above. In addition, the surface is assumed to be smooth

609   whilst in reality a complex topography of older lobe deposits and basin relief will affect the flows

610   (Prélat et al., 2009; Groenenberg et al., 2010; Spychala et al., 2016). Down-dip decrease in slope is

611   expected to decrease the flow capacity over the proximal lobe more rapidly than illustrated in the

612　scenarios of Figures 16 and 17. In addition, aggradational and erosional relief will introduce lateral

613　flow variability and lateral stacking variability (Prélat et al., 2009; Groenenberg et al., 2010).

614　*Constant drag coefficient.*

615　The ratio between drag at the upper surface and the bed on turbidity currents is recognised to vary

616　based on flow conditions (e.g., Parker et al., 1987; Sequeiros, 2012). However, the shift in relative

617　drag is commonly ignored in analyses, as it has been here. At low Richardson scales, mixing at the

618　top of the turbidity current is reduced, which reduces friction at the top when compared to friction at

619　the base of the flow (Kneller et al., in review). This balance is assumed to be constant in the usage of

620　Eq. 4. The bed shear stress is still decreasing monotonically with distance along the lobe, but at a

621　lower rate than the scenarios presented in Figures 16 and 17 when the balance of friction is allowed

622　to shift towards the bed with lower Richardson scales. The effect of this phenomenon is the delay of

623　flow transformation to a more distal location.

624　*Equal spreading over the lobe.*

625　The observed finger-like geometry of Fan 3 and the associated facies distribution is evidence for

626　focussed flow pathways (Rozman 2000; Rozman and Bouma 2000; Johnson et al., 2001; Hodgson et

627　al., 2006; Groenenberg et al., 2010). Consequently, the flow does not cover the lobe equally and

628　flow capacity will be higher along the pathways due to the higher amounts of sediment in

629　suspension, and increased flow velocity increasing the basal shear velocity. On the fringes of these

630　pathways it may be possible that lateral flow may undergo transformations (Spychala et al., in

631　revision).

632

633　**Flow transformation**

634

635　Reduction in the flow suspension capacity as described above may lead to the development of a

636　dense, cohesive lower boundary layer flow, where flows are primed to do so (abundance of clay

637　minerals and fine grained sediment). A steady, non-cohesive, low concentration turbidity current has

638　a given capacity, which drops as the flow decelerates (Hiscott, 1994). Accordingly, sediment falls

639　from suspension to the bed to form a grain framework, or 'rigid' bed which may or may not be

640　reworked depending upon the shear stress exerted by the flow on the bed. Sediment suspensions with

641　a significant cohesive and very fine-grained fraction behave differently and have the potential to

642   form fluid beds due to the high water content of clay flocs and fluid trapping by very fine-grained

643   non-cohesive sediment, which may allow the 'bed' to continue to flow (e.g., Winterwerp & Van

644   Kesteren, 2004). Silt and very fine sand may settle into the dense basal layer together with larger

645   clay flocs and other relatively large clasts and grains (mud clasts, micas, organic material). The

646   aggrading dense boundary layer flow, developed in the decelerating and progressively more

647   stratified flow, would therefore be saturated and cohesive, and given the appropriate conditions,

648   would be able to continue flowing downstream as a cohesive flow (rather than settling to form a

649   rigid bed). In such a flow, yield strength and buoyancy may become the primary particle support

650   mechanisms (e.g., Talling, 2013). McCave and Jones (1988) suggest that under these conditions

651   shearing at the lower boundary layer and continuous flux of the ambient fluid may flush the dense

652   lower layer breaking up clay flocs and pushing clay upwards in the flow or mobile deposit. This may

653   give rise to the development of a slightly better sorted thin lower layer, upon which the clay rich

654   suspension rides; and may explain the thin slightly better sorted layer present at the base of most of

655   the hybrid beds deposits documented here. Support for this comes from the presence of mud clasts

656   along intra-bed boundaries between basal relatively clean sandstone and overlying muddier

657   sandstones (e.g. Fig. 7E), suggesting that relative particle buoyancy may have played a role in the

658   lowermost part of the flow.

659

660

661   The minimum yield strength (τ_y) required to support a given grain size (d_{max}) within the inferred

662   transitional to laminar flows can be calculated, following Johnson (1970) and Hampton (1972,

663   1975):

$$d_{max} = \frac{8.4\tau_y}{(\rho_p - \rho_f)g}$$

664   (8)

665   Hampton (1972) demonstrated that this was a reliable approximation for sand particles submerged in

666   a clay-water matrix. To maintain laminar support of 125 μm quartz grains, that equates to a low

667   yield strength, 0.2 Pa. Flow concentrations in the range of 6% kaolin clay would be required to

668   generate the necessary yield strength to support 125 μm quartz grains; concentration is calculated by

669   rearranging Wan's (1982) formula:

$$\tau_y = 1280 \left(\frac{C}{100}\right)^3$$

670   (9)

671   The empirical formulation of Wan (1982) is only valid for kaolin flows, however, the petrological

672   analysis suggests that the primary clay was most-likely illite, which tends to form stronger bonds

673   than kaolin (see mineralogy section above). Shearing intensity decreases yield strength considerably

674   (Hampton, 1975), therefore the effect of shear stress on these flows also needs to be considered. For

675   example, Sumner et al. (2009) found that concentrations of approximately 14% kaolin were needed

676   to support very fine- to medium-grained sand (63-250 µm) in shearing clay-rich flows; similar

677   figures were suggested from the settling tube experiments of Amy et al. (2006). Additionally, Major

678   and Pierson (1992), in a series of experiments on sand-silt-clay slurries, noted that small changes in

679   sediment concentration, in the order of 2-4%, produced yield strength changes of up to an order of

680   magnitude. The minimum concentration estimate above (6% clay) is within the range of flow

681   concentrations considered by McCave & Jones (1988) (5-10%) for the generation of clay-silt yield

682   strength dominated flows; however the values of Sumner et al. (2009) (~14% clay; albiet kaolin) for

683   shearing fine-sand bearing flows are probably more appropriate.

684   The advection distance of these flows appears to be in the order of several kilometers, based

685   on bed length, suggesting that dewatering was a relatively slow process. Assuming that the laminar

686   flows intially have the flow velocity of their parent turbidity currents, e.g., for a 5% concentration

687   flow this might be in the region of 0.4 m/s (Figure. 16B), an advection distance of 4 km (from the 21

688   km 'transformtion point' to the lobe pinch-out) would suggest a dewatering time of c. 2.5 hours. In

689   all likelihood, the average flow velocity is significantly lower. A 0.2 m/s flow would suggest a

690   dewatering time of 5 hours. There is much local varibaility, which likely reflects subtle changes in

691   gradient and orientation with respect to palaeoflow.

692

Summary and comparison to 'long-distance transformation model'

694   The Fan 3 hybrid beds are related to events that entrained the substrate. Radial spreading of

695   individual flows and consequent deceleration caused the flow suspension capacity to be overcome,

696   and flows became transitional to laminar. Due to the high proportion of cohesive and fine material, a

697   dense low yield strength flowing layer formed, which progressively shut off the transfer of turbulent

698   kinetic energy from the base of the flow into the upper layers. Following this, the flows rapidly lost

699   energy and consequently come to a rest relatively abruptly, with the cleaner-lower and muddier-

700   upper deposits pinching out approximately contemporaneously. The transformation model is broadly

701   similar to that postulated by McCave and Jones (1988), and Talling's (2013) model 3. The principal

702   difference to Hodgson's (2009) 'D2' model is that the basal sandstones are here not considered to be

703   the product of forerunning turbidity currents, rather they are considered to be the product of distal

704   flow collapse and transformation, although both models rely on incorporation of substrate material

705   updip. As demonstrated by the numerical model, deceleration alone may result in flow

706   transformation (Model 3 of Talling, 2013), but in this case the evidence shows that many of the

707   flows depositing hybrid beds behaved erosively updip when they were undersaturated ($\Gamma > 1$), and

708   through deceleration became saturated ($\Gamma < 1$) and transformed to transitional-laminar flows.

709   Transformation appears to be a general characterisitc of decelerating clay-rich flows (Talling, 2013).

710   If the coarser fraction of the flow has not completely settled at the point where viscous forces begin

711   to dominate, these grains will be incorporated into the higher strength flow (Talling, 2013). In the

712   case of the style of distal beds outlined here, and seen elsewhere in systems of a similar grain size,

713   (e.g, the Wilcox Fm. Zarra et al., 2007; Kane & Pontén, 2012), the low settling velocity of the very

714   fine-grained sand and coarse silt, may make these type of deposits common. This is for two reasons:

715   1) coarser grained flows may undergo sedimentation earlier, without time for the transformation to

716   occur; 2) coarser or denser grains require greater tubulent energy to be supported, and this may

717   inhibit the formation of clay bonds. Consequently, in coarser-grained systems lacking the fine tail,

718   these types of hybrid beds may not develop.

719

Conclusions

721   A downstream transition from turbidite-dominated stratigraphy to mixed turbidites and hybrid beds

722   is documented. Hybrid beds from the distal parts of Fan 3 stratigraphy are characterised and placed

723   within a physical model based on application of the suspension capacity parameter, Γ. Flow

724   transformation is inferred to take place through:

725   1. Erosion and entrainment by turbidity currents of clay, silt and very fine sand in the

726   channel to channel-lobe transition zone areas when flows are undersaturated ($\Gamma > 1$)

727

728   2. Deceleration of flows is associated with radial spreading from the lobe apex, reduction in

729   bed shear stress and accordingly a reduction in suspension capacity; we present a simple

730   model for estimation of this.

731

732   3. Formation of a low yield-strength cohesive basal layer, which flows in a transitional to

733   increasingly laminar manner that allows settling of the denser/coarser grained fraction.

734

735   4. The rising yield strength of the lower layer inhibits the efficiency of vertical mixing,

736   leading to a collapse of the turbulent energy field and en-masse transformation of the

737   upper part of the flow. This results in a thick argillaceous sandstone division containing

738   the residual material within the flow (sand, silt, clay, organics, mica grains).

739

740   The fine-grained nature of the Fan 3 gravity flow system may have promoted the development of

741   these types of flows, with the fine suspended load transforming to low yield-strength driven flows

742   following loss of suspension capacity; this is potentially the reason that very similar facies are found

743   in other systems of similar grain size range (e.g., Ross Fm., e.g., Pyles & Jennette. (2009), Wilcox

744   Fm., e.g., Zarra (2007)).

745   Flow transformation is here considered to be localised, occurring due to autocyclic evolution of

746   radially decelerating flows, rather than a long runout process with the constituent parts dividing into

747   a forerunning turbidity current and trailing debris flow (Haughton et al., 2003; 2009; Hodgson,

748   2009); whilst those models are valid, the model presented herein provides a mechanism for the

749   development of transitional to laminar flows from an initial turbulent flow, and a particular class of

750   layered hybrid bed which seem to dominate fan fringes in fine-grained systems.

751

References

Amy, L.A. and Talling, P.J. (2006) Anatomy of turbidites and linked debrites based on long distance (120 × 30 km) bed correlation, Marnoso Arenacea Formation, Northern Apennines, Italy. Sedimentology, **53**, 161-213.

Amy, L.A., Talling, P.J., Edmonds, V.O., Sumner, E.J. and Lesueur, A. (2006) An experimental investigation of sand–mud suspension settling behaviour: implications for bimodal mud contents of submarine flow deposits. Sedimentology, **53**, 1411–1434.

Baas, J.H., Hailwood, E.A., McCaffrey, W.D., Kay, M., and Jones, R. (2007) Directional petrological characterisation of deep-marine sandstones using grain fabric and permeability anisotropy: methodologies, theory, application and suggestions for integration. *Earth-Science Reviews*, **82**, 101–142.

Baas, J.H., Best, J.L., Peakall, J., and Wang, M. (2009) A phase diagram for turbulent, transitional and laminar clay suspension flows. *Journal of Sedimentary Research*, **79**, 162–183, doi:10.2110/jsr.2009.025.

Baas, J.H., Best, J.L., and Peakall, J. (2011) Depositional processes, bedform development and hybrid bed formation in rapidly decelerated cohesive (mud–sand) sediment flows. *Sedimentology*, 58, 1953–1987. doi:10.1111/j.1365-3091.2011.01247.x.

Barker, S.P., Haughton, P.D.W., McCaffrey, W.D., Archer, S.G., and Hakes, B. (2008) Development of rheological heterogeneity in clay-rich high-density turbidity currents: Aptian

787   Britannia Sandstone Member, U.K. Continental shelf. *Journal of Sedimentary Research*, 78, 45–68,

788   doi:10.2110/jsr.2008.014.

789

790   **Bouma, A.H.** (1962) *Sedimentology of some flysch deposits: A graphic approach to facies*

791   *interpretation*. Elsevier, Amsterdam, 168 pp.

792

793   **Bouma, A.H. and Wickens, H.D.** (1991) Permian passive margin submarine fan complex, Karoo

794   Basin, South-Africa: possible model to Gulf of Mexico. *Transacations-Gulf Coast Association of*

795   *Geological Societies*, **41,** 30-42.

796

797   **Cantero, M. I., Balachandar, S. and Parker, G.** (2009), Direct numerical simulation of

798   stratification effects in a sediment- laden turbulent channel flow, *Journal of Turbulence*, 10, 37–41.

799

800   **Cantero, M.I., Cantelli, A., Pirmez, C., Balachandar, S., Mohrig, D., Hickson, T.A., Yeh, T-H.,**

801   **Naruse, H. and Parker, G.** (2012) Emplacement of massive turbidites linked to extinction of

802   turbulence in turbidity currents. *Nature Geoscience*, **5**, 42-45.

803

804   **Cantero, M. I., Shringarpure, M. and Balachandar, S.** (2012), Towards a universal criteria for

805   turbulence suppression in dilute turbidity currents with non-cohesive sediments. *Geophysical*

806   *Research Letters*, **39**, L14603.

807

808   **Cole, D.I.** (1992) Evolution and Development of the Karoo Basin. *Inversion Tectonics of the Cape*

809   *Fold Belt, Karoo and Cretaceous Basins of Southern Africa***,** 87-99.

810

811   **Coulson, J.M. and Richardson, J.F.** (1991) Chemical Engineering Vol. 2. Butterworth Heinemann,

812   Oxford. 1183p.

813

814   **Dapples, E.C., and Rominger, J.F.** (1945) Orientation analysis of fine-grained clastic sediments: a

815   report of progress. *Journal of Geology*, **53**, 246–261.

816

817   **DeCelles, P.G. and Giles, K.A.** (1996) Foreland basin systems. *Basin Research*, **8,** 105-123.

818

819   **De Leeuw, J., Eggenhuisen J.T. and Cartigny, M.J.B.** (2016) Morphodynamics of submarine

820   channel inception revealed by new experimental approach. Nature Communication, **7**:10886 doi:

821   10.1038/ncomms10886

822   **De Wit, M.J., and Ransome, I.G.D.** (1992) Regional inversion tectonics along the southern margin

823   of Gondwana. In: Inversion Tectonics of the Cape Fold Belt, Karoo and Cretaceous Basins of

824   Southern Africa. In De Wit, M.J., and Ransome, I.G.D. Rotterdam, Balkema, p. 15–21.

825

826   **El-Gawad, S. Abd., Cantelli, A., Pirmez, C., Minisini, D., Sylvester, Z. and Imran, J.** (2012)

827   Three-dimensional numerical simulation of turbidity currents in a submarine channel on the seafloor

828   of the Niger Delta slope. Journal of Geophysical Research, 117, C05026.

829

830   **Eggenhuisen, J.T., Cartigny, M.J.B. and de Leeuw, J.** (2016). Physical theory for near-bed

831   turbulent particle-suspension capacity. Earth Surface Dynamics Discussion, doi:10.5194/esurf-2016-

832   33.

833

834   **Fildani A., Weislogel A.,Drinkwater N.J., McHargue T., Tankard A., Wooden J., Hodgson D.,**

835   **Flint S.** (2009) U-Pb zircon ages from the southwestern Karoo Basin, South Africa—Implications

836   for the Permian-Triassic boundary. *Geology*, **37**, 719–722. doi: 10.1130/G25685A.1.

837

838   **Fildani, A., Weislogel, A., Drinkwater, N.J., McHargue, T., Tankard, A., Wooden, J., Hodgson,**

839   **D. and Flint, S.** (2009) U-Pb zircon ages from the southwestern Karoo Basin, South Africa-

840   Implications for the Permian-Triassic boundary. *Geology*, **37,** 719-722.

841

842   **Folk, R.L., Andrews, P.B. and Lewis, D.W.** (1974) Detrital sedimentary rock classification and

843   nomenclature for use in New Zealand. *New Zealand Journal of Geology and Geophysics*, **13**, 937-

844   968.

845

846   **Fonnesu, M., Haughton, P., Felletti, F., and McCaffrey, W.** (2015) Short length-scale variability

847   of hybrid event beds and its applied significance. *Marine and Petroleum Geology, 67, 583-603.*

848

849   **Goldhammer, R.K., Wickens, H.DeV., Bouma, A.H., and Wach, G.** (2000) Sequence

850   stratigraphic architecture of the Late Permian Tanqua submarine fan complex, Karoo Basin, South

851   Africa, in Bouma, A.H., and Stone, C.G., eds., Fine-Grained Turbidite Systems: American

852   Association of Petroleum Geologists, Memoir 72, and SEPM, Special Publication 68, p. 165–172.

853

854   **Groenenberg, R.M., Hodgson, D.M., Prelat, A., Luthi, S.M. and Flint, S.S.** (2010) Flow-Deposit

855   Interaction in Submarine Lobes: Insights from Outcrop Observations and Realizations of a Process-

856   Based Numerical Model. *Journal of Sedimentary Research*, **80,** 252-267.

857

858   **Grundvåg, S.A., Johannessen, E.P., Helland-Hansen, W. and Plink-Björklund, P.** (2014)

859   Depositional architecture and evolution of progradationally stacked lobe complexes in the Eocene

860   Central Basin of Spitsbergen. *Sedimentology*, **61**, 535-569.

861   **Hampton, M.A.** (1972) The role of subaqueous debris flow in generating turbidity currents. Journal

862   of Sedimentary Petrology, **42**, 775–793.

863

864   **Hampton, M.A.** (1975) Competence of fine grained debris flows. Journal of Sedimentary Petrology,

865   **45**, 833–844.

866

867   **Haughton, P.D.W., Barker, S.P. and McCaffrey, W.D.** (2003) 'Linked' debrites in sand-rich

868   turbidite systems - origin and significance. *Sedimentology*, **50,** 459-482.

869

870   **Haughton, P., Davis, C., McCaffrey, W. and Barker, S.** (2009) Hybrid sediment gravity flow

871   deposits - Classification, origin and significance. *Marine and Petroleum Geology*, **26,** 1900-1918.

872

873   **Hiscott, R.N., and Middleton, G.V.** (1980) Fabric of coarse deep-water sandstones, Tourelle

874   Formation, Quebec, Canada: Journal of Sedimentary Petrology, 50, 703–722.

875

876   **Hiscott, R.N.** (1994) Loss of capacity, not competence, as the fundamental process governing

877   deposition from turbidity currents. *Journal of Sedimentary Research*, A64, 209–214.

878

879   **Hodgson, D., Flint, S.S., Hodgetts, D., Drinkwater, N.J., Johannessen, E.P. and Luthi, S.M.**

880   (2006) Stratigraphic evolution of fine-grained submarine fan systems, Tanqua depocenter, Karoo

881   Basin, South Africa. *Journal of Sedimentary Research*, **76,** 20-40.

882

883   **Hodgson, D. (**2009**)** Distribution and origin of hybrid beds in sand-rich submarine fans of the

884   Tanqua depocentre, Karoo Basin, South Africa. *Marine and Petroleum Geology*, **26**, 1940–1956,

885   doi:10.1016/j.marpetgeo.2009.02.011.

886

887   **Hodgson, D., Kane, I., Flint, S., Brunt, R., Ortiz-Karpf, A.** (2016). Time transgressive

888   confinement on the slope and the progradation of basin-floor fans: Implications for the sequence

889   stratigraphy of deep-water deposits. *Journal of Sedimentary Research*, 86, 73-86.

890

891   **Hofstra, M. Hodgson, D.M. Peakall, J.; Flint, S.S.** (2015) Giant scour-fills in ancient channel-lobe

892   transition zones: Formative processes and depositional architecture. *Sedimentary Geology*, Volume

893   329, 98-114.

894

895   **Ito, M.** (2008) Downfan transformation from turbidity currents to debris flows at a

896   channel-to-lobe transitional zone: the lower Pleistocene Otadai Formation, Boso Peninsula, Japan.

897   *Journal of Sedimentary Research*, **78**, 668–682.

898

899   **Johnson, A.** (1970) Physical Processes in Geology, W. H. Freeman, New York. 577 p.

900

901   **Johnson, M.R.** (1994) Thin section grain size analysis revisited. *Sedimentology*, **41**, 985–999.

902

903   **Johnson, S.D., Flint, S., Hinds, D. and Wickens, H.D.** (2001) Anatomy, geometry and sequence

904   stratigraphy of basin floor to slope turbidite systems, Tanqua Karoo, South Africa. *Sedimentology*,

905   **48,** 987-1024.

906

907   **Kane, I.A., McCaffrey, W.D., and Peakall, J.** (2010a) On the origin of palaeocurrent complexity

908   within deep marine channel levees. Journal of sedimentary Research, **80**, 54-66.

909

910   **Kane, I.A., McCaffrey, W.D., Peakall, J. and Kneller, B.C.** (2010b). Submarine channel levee

911   shape and sediment waves from physical experiments. *Sedimentary Geology*, 223, 75-85.

912

913   **Kane, I.A. and Pontén, A.S.M.** (2012) Submarine transitional flow deposits in the Paleogene Gulf

914   of Mexico. *Geology*, **40,** 1119-1122.

915

916   **Khelifa, A. and Hill, P.S.** (2006) Models for effective density and settling velocity of clay flocs.

917   *Journal of Hydraulic Research*, **44**, 390-401.

918

919   **King, R.C.** (2005) *Structural evolution of the Cape Fold Belt; implications for sediment routing to*

920   *the SW Karoo Basin*, University of Liverpool, Unpublished, 327 pp.

921

922   **King, R.C., Hodgson, D.M., Flint, S.S., Potts, G.J. and Van Lente, B.** (2009) Development of

923   subaqueous fold belt as a control on the timing and distribution of deepwater sedimentation: An

924   example from the Southwest Karoo Basin, South Africa. In: Kneller, B., Martinsen, O.J., McCaffrey,

925   B. (Eds.), External Controls on Deep-Water Depositional Systems. *SEPM Special Publication,* **92**,

926   261-278.

927

928   **Kneller, B. C.** (1995) Beyond the turbidite paradigm: physical models for deposition of turbidites

929   and their implications for reservoir potential. In: Characterization of Deep Marine Systems (Eds A.J.

930   Hartley and D.J. Prosser), Geol. Soc. Spec. Publ., **94**, 31–49.

931

932   **Kneller, B.C.** 2003. The influence of flow parameters on turbidite slope channel architecture.

933   *Marine and Petroleum Geology*, **20**, 901–910.

934

935   **López-Gamundí and Rossello, E.A.** (1998) Basin fill evolution and paleotectonic patterns along

936   the Samfrau geosyncline: the Sauce Grande basin–Ventana foldbelt (Argentina) and Karoo basin-

937   Cape foldbelt (South Africa) revisited. *Geologische Rundschau* **86,** 819-934.

938

939   **Lowe, D.R.** (1982) Sediment gravity flows: II. Depositional models with special reference to the

940   deposits of high-density turbidity currents. *Journal of Sedimentary Petrology*, **52**, 279-297.

941

942   **Lowe, D.R. and Guy, M.** (2000) Slurry-flow deposits in the Britannia Formation (Lower

943   Cretaceous), North Sea: a new perspective on the turbidity current and debris flow problem.

944   *Sedimentology*, **47,** 31-70.

945

946   **Luthi, S.M., Hodgson, D.M., Geel, C.R., Flint, S.S., Goedbloed, J.W., Drinkwater, N.J.,**

947   **Johanessen, E.P.** (2006) Contribution of research borehole data to modelling fine-grained turbidite

948 reservoir analogues, Permian Tanqua-Karoo basin floor fans (South Africa). *Petroleum Geology*, **12**,

949 175–190.

950

951 **McCave, I.N. and Jones, K.P.N.** (1988) Deposition of ungraded muds from high-density non-

952 turbulent turbidity currents. *Nature,* **133**, 250-252.

953

954 **Major, J.J. and Pierson, T.C.** (1992) Debris Flow Rheology: Experimental analysis of fine-grained

955 slurries. *Water Resources Research*, **28**, 841-857.

956

957 **Martinsen, O. J., T. Lien, and R. G. Walker** (2000) Upper Carboniferous deep water sediments,

958 western Ireland: analogues for passive margin turbidite plays**,** in P. Weimer, R. M. Slatt, J. Coleman,

959 N. C. Rossen, H. Nelson, A. H. Bouma, M. J. Styzen, and D. T. Lawrence, eds., Deep-water

960 reservoirs of the world, Gulf Coast Section-SEPM Special Publication, p. 533-555.

961

962 **McKay, M.P., Weislogel, A.L., Fildani, A., Brunt, R.L, Hodgson, D.M. and Flint, S.S.** (2015)

963 U–Pb zircon tuff geochronology from the Karoo Basin, South Africa: implications of zircon

964 recycling on stratigraphic age controls. *International Geology Review*, **57**, 393–410.

965

966 **Moiola, R.J. and Weiser, D.** (1968) Textural parameters: An Evaluation. *Journal of Sedimentary*

967 *Petrology*, **38**, 45-53.

968

969 **Mohrig, D., and Buttles, J.,** 2007, Deep turbidity currents in shallow channels. *Geology*, v. 35, p.

970 155–158.

971

972 **Morris, W.R., Scheilhing, M.H., Wickens, DeV., Bouma, A.H.** (2000) Reservoir architecture of

973 deepwater sandstones: examples from the Skoorsteenberg Formation, Tanqua Karoo Sub-Basin,

974 South Africa. In: P. Weimer, R.M. Slatt, A.H. Bouma, and D.T. Lawrence, eds., Deep-water

975 reservoirs of the world: Gulf Coast Section SEPM Foundation, Twentieth Annual Research

976 Conference, p. 1010-1032.

977

978 **Mutti, E. and Sonnino, M.** (1981) Compensational cycles: a diagnostic feature of turbidite

979 sandstone lobes. International Association of Sedimentologists 2nd European Meeting, Bologna,

980 Italy, 120-123.

981

982 **Parker, G., M. García, Y. Fukushima, and W. Yu** (1987), Experiments on turbidity currents over

983 an erodible bed. Journal of Hydraulic Research, **25**, 123–147.

984

985 **Piper, D.J.W., and Normark, W.R.** (1983) Turbidite depositional patterns and flow characteristics,

986 Navy submarine fan, California Borderland. *Sedimentology*, **30**, 681–694.

987

988 **Pirrie, D., Butcher, A.R., Power, M.R., Gottlieb, P., Miller, G.L**. (2004), "Rapid quantitative

989 mineral and phase analysis using automated scanning electron microscopy (QEMSCAN®); potential

990 applications in forensic geoscience". In: Pye, K., Croft, D.J. (Eds.), Forensic Geoscience, Principles,

991 Techniques and Applications, Vol. 232. Geological Society Special Publication, London, pp 23–136.

992

993 **Pope, S.B.** (2000) *Turbulent Flows.* Cambridge University Press, Cambridge, UK, 771 pp.

994

995 **Porten, K.W., Kane, I.A., Warchoł, M.J. and Southern, S.J.,** in press. A sedimentological

996 process-based approach to depositional reservoir quality of deep-marine sandstones: an example

997 from the Springar Formation, north-western Vøring Basin, Norwegian Sea. *Journal of Sedimentary*

998 *Research*.

999

1000 **Poyatos-More, M., Jones, G. D., Brunt, R., David M. Hodgson, Richard J. Wild, & Flint,**

1001 **S.** (2016). Mud-dominated basin margin progradation: processes and implications. *Journal of*

1002 *Sedimentary Research*, **86**, 863-878.

1003

1004 **Prélat, A. and Hodgson, D.M.** (2013) *The full range of turbidite bed thickness patterns in*

1005 *submarine lobes: controls and implications***.** Journal of the Geological Society, **170**, 209-214.

1006

1007 **Prélat, A., Hodgson, D.M. and Flint, S.S.** (2009) Evolution, architecture and hierarchy of

1008 distributary deep-water deposits: a high-resolution outcrop investigation from the Permian Karoo

1009 Basin, South Africa. *Sedimentology*, 56, 2132-U25.

1010

1011 **Pyles, D.R. and Jennette, D.C.** (2009) Geometry and architectural associations of co-genetic

1012 debrite–turbidite beds in basin-margin strata, Carboniferous Ross Sandstone (Ireland): Applications

1013   to reservoirs located on the margins of structurally confined submarine fans. *Marine and Petroleum*

1014   *Geology*, **26,** 1974-1996.

1015

1016   **Pysklywec, R.N. and Mitrovica, J.X**. (1999) The role of subduction-induced subsidence in the

1017   evolution of the Karoo Basin. *The Journal of Geology,* **107**, 155-164.

1018

1019   **Sequeiros, O.E.** (2012) Estimating turbidity current conditions from channel morphology:A Froude

1020   number approach. *Journal of Geophysical Research*, **117**, C04003.

1021

1022   **Smith, R.H.M.** (1990) A review of stratigraphy and sedimentary environments of theKaroo basin of

1023   South Africa. *Journal of African Earth Sciences*, **10**, 117–137.

1024

1025   **Southern, S.J., Patacci, M., Felletti, F. and McCaffrey, W.D.** (2015) Influence of flow

1026   containment and substrate entrainment upon sandy hybrid event beds containing a co-genetic mud-

1027   clast-rich division. *Sedimentary Geology*, **321**. 105 - 122.

1028

1029   **Southern, S.J., Kane, I.A., Warchoł, M.J., Porten, K.W. and McCaffrey, W.D.** (2016) Hybrid

1030   event beds dominated by transitional-flow facies: Character, distribution and significance in the

1031   Maastrichtian Springar Formation, north-west Vøring Basin, Norwegian Sea. ***Sedimentology***,

1032   DOI: 10.1111/sed.12323

1033

1034   **Spychala, Y.T, Hodgson, D.M., Stevenson, C.J. and Flint, S.S.** (2016) Aggradational lobe fringes:

1035   The influence of subtle intrabasinal seabed topography on sediment gravity flow processes and lobe

1036   stacking patterns. *Sedimentology*. DOI: 10.1111/sed.12315

1037

1038   **Spychala, Y.T., Hodgson, D.M., Prelat, A., Kane, I.A., Flint, S.S. and Mountney, N.P.** (in press),

1039   Frontal and lateral submarine lobe fringes: Comparing sedimentary facies, architecture and flow

1040   processes. Journal of Sedimentary Research.

1041

1042

1043 **Stevenson, C.J., Jackson, C.A.L., Hodgson, D.M., Hubbard, S.M., and Eggenhuisen, J.T.** 2015,
1044 Deep-water sediment bypass. *Journal of Sedimentary research*, 85, 1058-1081.

1045

1046 **Sullivan, M.D., Jensen, G.N., Goulding, F.J., Jennette, D.C., Foreman, J.L. and Stern, D.**
1047 (2000) Architectural analysis of deep-water outcrops: Implications for exploration and production of
1048 the Diana Sub-basin, western Gulf of Mexico, *in* P. Weimer, R.M. Slatt, A.H. Bouma, and D.T.
1049 Lawrence, eds., Deep-water reservoirs of the world: Gulf Coast Section SEPM Foundation,
1050 Twentieth Annual Research Conference, p. 1010-1032.

1051

1052 **Sumner, E.J., Talling, P.J., and Amy, L.A. (**2009) Deposits of flows transitional between turbidity
1053 current and debris flow. Geology, **37**, 991–994, doi:10.1130/G30059A.1.

1054

1055 **Sylvester, Z. and Lowe, D.R.** (2004) Textural trends in turbidites and slurry beds from the
1056 Oligocene flysch of the East Carpathians, Romania. Sedimentology, **51**, 945-972.

1057

1058 **Talling, P.J., Amy, L.A., Wynn, R.B., Peakall, J. and Robinson, M.** (2004) Beds comprising
1059 debrite sandwiched within co-genetic turbidite: origin and widespread occurrence in distal
1060 depositional environments. *Sedimentology*, **51,** 163-194.

1061

1062 **Talling, P.J., Masson, D.G., Sumner, E.J**. and **Malgesini, G.** (2012) Subaqueous sediment density
1063 flows: Depositional processes and deposit types. *Sedimentology*, **59**, 1937-2003.

1064

1065 **Talling, P.J.** (2013) Hybrid submarine flows comprising turbidity current and cohesive debris flow:
1066 Deposits, theoretical and experimental analyses, and generalized models: Geosphere, 9, 1-28.

1067

1068 **Tankard A., Welsink H., Aukes P., Newton R., Stettler E.** (2009) Tectonic evolution of the Cape
1069 and Karoo basins of South Africa. *Marine and Petroleum Geology*, **26**, 1379–1412. doi:
1070 10.1016/j.marpetgeo.2009.01.022.

1071

1072

1073 **Terlaky, V., Arnott, R.W.C.** (2014) Matrix-rich and associated matrix-poor sandstones: avulsion
1074 splays in slope and basin-floor strata. Sedimentology 61, 1175-1197.
1075 http://dx.doi.org/10.1111/sed.12096.

1076

1077 **Twichell, D., Nelson, C.H., Kenyon, N. and Schwab, W**. (2009) The Influence of External

1078 Processes on the Holocene Evolution of the Mississippi Fan, *in* B. Kneller, O.J. Martinsen, and B.

1079 McCaffrey, eds., External Controls on Deep-Water Depositional: SEPM Special Publication **92**,

1080 145-157.

1081

1082 **van der Werff, W. and Johnson, S.** (2003a) High resolution stratigraphic analysis of turbidite

1083 system, Tanqua Karoo Basin, South Africa. *Marine and Petroleum Geology*, **20,** 45-69.

1084

1085 **van der Werff, W. and Johnson, S.D.** (2003b) Deep-sea fan pinch-out geometries and their

1086 relationship to fan architecture, Tanqua Karoo basin (South Africa). *International Journal of Earth*

1087 *Sciences*, **92,** 728-742.

1088

1089 **Veevers, J.J., Cole, D.I. and Cowan, E.J.** (1994) Souther Africa: Karoo Basin and Cape Fold Belt.

1090 In: *Permian-Triassic Pangean Basins and Foldbelts Along the Panthalassan Marginof*

1091 *Gondwanaland* (Eds J.J. Veevers and C.M. Powekk), **Memoir 184**, pp. 223-279. Geological Society

1092 of America.

1093

1094 **Visser, J.N.J.** (1997) Deglaciation sequences in the Permo-Carboniferous Karoo and Kalahari

1095 basins of the southern Africa: a toll in the analysis of cyclic glaciomarine basin fills. *Sedimentology,*

1096 **44**, 507-521.

1097

1098 **Visser, J.N.J. and Prackelt, H.E.** (1996) Subduction, mega-shear systems and Late Palaeozoic

1099 basin development in the African segment of Gondwana. *Geologische Rundschau,* **85**, 632-646.

1100

1101 **Wan, Z.** (1982) Bed Material Movement in Hyperconcentrated Flow. Institute of Hydrodynamics

1102 and Hydraulic Engineering, Technical University of Denmark, Lyngby, Series Paper, pp. 16–24.

1103

1104 **Wickens, H.J.** (1994) *Basin floor fan building turbidites of the southwestern Karoo Basin, Permian*

1105 *Ecca Group, South Africa*, University of Port Elizabeth, Unpublished, 233 pp.

1106

1107 **Wild, R., Hodgson, D. and Flint, S.** (2005) Architecture and stratigraphic evolution of multiple,

1108 vertically-stacked slope channel complexes, Tanqua depocentre, Karoo Basin, South Africa. In:

1109   *Submarine slope systems: processes and products* (Eds D. Hodgson and S. Flint), **244**, pp. 89-111.

1110   The Geological Society of London, London.

1111

1112   **Wild, R., Flint, S.S. and Hodgson, D.M.** (2009) Stratigraphic evolution of the upper slope and shelf

1113   edge in the Karoo Basin, South Africa. *Basin Research*, **21,** 502-527.

1114

1115   **Wintwerp, J.C., and van Kesteren, W.G.M.** (2004). Introduction to the Physics of Cohesive

1116   Sediment in the Marine Environment: Oxford, U.K., Elsevier, Developments in Sedimentology 56,

1117   559 p.

1118

1119   **Wood, A. and Smith, A., J.,** (1958) The Sedimentation and Sedimentary History of the

1120   Aberystwyth Grits (Upper Llandoverian). *Quarterly Journal of the Geological Society*, **114,** 163-

1121   195.

1122

1123   **Zarra, L**., (2007) Chronostratigraphic Framework for the Wilcox Formation (Upper Paleocene-

1124   Lower Eocene) in the Deep-Water Gulf of Mexico: Biostratigraphy, Sequences, and Depositional

1125   Systems. In: Kennan, L., Pindell, J., and Rosen, N.C., eds., The Paleogene of the Gulf of Mexico and

1126   Caribbean Basins: Processes, Events, and Petroleum Systems: GCSSEPM Foundation 27th Annual

1127   Bob F. Perkins Research Conference, p. 81−145.

1128   **Zhiyao, S., Tingting, W., Fumin, X. and Ruijie, L.** (2008). A simple formula for predicting

1129   settling velocity of sediment particles. *Water Science and Engineering Journal*, **1**, 37− 43.

1130

1131   **Table & Figure Captions**

1132   Table 1. Mineralogical composition of samples analysed using QEMSCAN. Heavy outlines mark individual

1133   beds, which are classified here as hybrid beds (HB), turbidites (TURB) and thick amalgamated sandstone –

1134   see text (AMAL), the lowermost and uppermost samples for each bed are marked (-base and -top

1135   respectively).

1136

1137   Table 2. Grain fabric data. Heavy outlines mark individual beds, which are classified here as HB (hybrid

1138   bed), TURB (turbidite) and AMAL (thick amalgamated sandstone – see text).

1139

1140   Figure 1. A) Aerial image of part of South Africa, highlighting the location of the Tanqua

1141   Depocentre, approximately 90 km northwest of the town of Laingsburg. B) Outline of Fan 3 in the

1142   Tanqua Depocentre (from Hodgson et al., 2006); the field area is boxed and expanded in 'D' and

1143   'E'. Blue arrows show the general palaeoflow trends. C) Aerial image of the field area, illustrating

1144   the outcrop continuity of the near horizontal bedding surfaces, and the location of the measured

1145   sections. D) Schematic stratigraphic log of the Permian to earliest Triassic deep-marine to fluvial fill

1146   of the Tanqua depocentre (modified from Wild et al., 2005). E) Simple geological map illustrating

1147   the position of Fan 3 (bold line) and stratigraphic packages between fan tops. At this scale the fan

1148   tops are the only mappable surfaces, as the fans tend to weather into steep outcrop faces, whereas the

1149   finer-grained inter-fans form gentler slopes. The sandy part of Fan 2 has pinched out in this area

1150   (pinching out to the north), and is beneath the resolution of this map; Fan 1 has pinched out. The

1151   uppermost package, i.e., 'Top Unit 5 and younger', is predominantly the Kookfontein Fm.

1152   Figure 2. A) Correlation panel of 1:20 outcrop logs SK1-20; positions of 1:2 logs are shown

1153   alongside the relevant log. The correlations are based on walking out key stratigraphic surfaces, the

1154   lobes stack to form a lobe complex (Fan 3). Note that lobes 1 and 3 have pinched out in this position.

1155   The outcrop panel (B) shows the general character and exposure of the distal parts of Fan 3. C, D

1156   and E illustrate the general outcrop character at the positions of logs SK11, SK9 and SK7

1157   respectively. The yellow and grey colouring gives a general indication of the sandstone (yellow) and

1158   mudstone (grey) distribution. Palaeoflow is to the north, approximately right to left in the image.

1159   Figure 3. (A) Correlation panel of logged sections from behind outcrop boreholes, spanning Fan 3

1160   from the proximal channel-dominated part (Ongeluks River outcrops), to the channel-lobe transition

1161   and across the lobe to the distal parts studied here (e.g., Boreholes NB2-NS1). Note that the

1162   environments indicated are at the point of the arrows, not spanning the entire fan at that location.

1163   Correlations are tentative owing to the complex nature of compensational lobe stacking patterns and

1164   based on finer-grained intervals subdividing the sandstone rich element, following Prélat et al., 2009.

1165   A clear facies trend is observed across the lobe complex, illustrated by the plan view image (B).

1166   Figure 4. Sedimentary logs through Fan 3, positions shown in Figure 1.

1167   Figure 5. Detailed sedimentary logs from Fan 3, positions shown in Figure 1.

1168   Fig. 6. Representative turbidite facies. A) Thick bedded turbidite with a sharp base, weak normal
1169   grading and with a clast-rich upper part; clasts are partly disaggregated generating clay-rich patches
1170   within the sandstone. B) Erosional bed bases typically plane out on mudstones and cut downwards in
1171   a stepwise manner through thin-bedded intervals, occasionally with contemporaneous lateral
1172   injection. C) Erosional step at base of medium-bedded sandstone which is loaded into underlying
1173   thin-bedded silty turbidites. D) Thin-bedded very-fine-grained low-density turbidites. E) Rippled bed
1174   top to low density turbidite. F) Plant imprints in an intra-bed division.

1175   Fig. 7. Representative hybrid bed photographs ('B' and 'T' symbols indicate base and top of beds).
1176   A) Bed showing intense interaction with the substrate and muddy upper part, these are typical in
1177   medial lobe settings. B & C) Hybrid beds with thick laminar/ high concentration flow deposits in
1178   their upper parts; these are typical in medial to distal settings. D) Hybrid beds with large rafts of
1179   siltstone and mudstone. E & F) Thin hybrid beds characteristic of the distal facies, with thin
1180   relatively clean sands at bed bases and overlying layers of varying mud content.

1181   Figure 8. Photographs from cores of representative facies. A) Thin-bedded low-density turbidites; B)
1182   Thinly-interbedded low-density turbidites dominated by planar-lamination (i), small-scale load and
1183   flame structures (ii), and ripple-cross lamination (iii). C) Silty low-density turbidites graded from
1184   medium silt (i) to very-fine silt (ii). D) Turbidite with loading and injection of the substrate at the
1185   base. The upper part of the bed is truncated (i). E) Detail of loading and deformation at the base of a
1186   turbidite. F) Muddy sandstone truncated by an erosion surface overlain by claystone (bypass surface)
1187   and overlain by an argillaceous sandstone. G) Small injectite extending from a bed top. H)
1188   Dewatering pillars in the upper part of a hybrid bed, (ii) large mudstone clasts. I) Thick debrite with
1189   cleaner sandstone 'balls' and injections in an overall muddy sand matrix.

1190   Fig. 9. Quartz-feldspar-lithics (QFL) plot for samples subdivided into 'turbidites' and 'hybrid beds.
1191   Turbidites fall entirely within the lithic arkose class, whilst hybrid beds span the lithic arkose and
1192   feldspathic litharenite classes. Ternary plot from Folk (1974).

1193   Figure 10. Mineral maps from thin-sections, based on chemical composition data from QEMSCAN.
1194   A-F show samples SK7A, B, C, D, H and I respectively. SK7A-D are interpreted as hybrid beds
1195   whilst SK7H and SK7I are interpreted as turbidites (see table 1).

1196   Figure 11. Representative thin-section photomicrographs. A) Sample SK7B: clay-rich sample from

1197   the middle part of a hybrid bed. Note the organic fragments and porosity (blue) due to dissolution of

1198   framework minerals (probably feldspar). B) Sample SK7C: from the middle division of a hybrid bed,

1199   this clay-rich sandstone has a strong bed-parallel grain fabric, with aligned claystone and organic

1200   clasts. C) Sample SK7D: Sample from a thick muddy division within a hybrid bed, note the strong

1201   grain fabric with lens of coarser-grained sediment in the centre of the image. The sample lacks

1202   visible porosity. D) Sample SK7E: Mixed 'swirled' fabric of relatively finer- and coarser-grained

1203   lenses. This sample is from a lighter coloured band in a hybrid bed. The large rounded clast is a

1204   claystone. Note the porosity due to grain dissolution. E) Sample SK7H: This sample is from a

1205   tractional sandstone with weak plane-parallel lamination, which has a much lower mud content than

1206   the previous examples, and an alignment of quartz and feldspar grains along laminae. F) Sample

1207   SH7I. This sample is from the very-thick bed which caps Fan 3 at the SK7 locality. It does not

1208   appear to have a strong grain fabric in thin-section and in outcrop lacks obvious tractional structure.

1209   The visible porosity is most-likely related to weathering processes and fracturing around coarser

1210   grains.

1211   Figure 12. Thin-section photomicrographs in plane polarized light, from an argillaceous sandstone

1212   division of a hybrid bed (Sample SK7A, Log SK7. A) Illustration of the very low degree of porosity

1213   in these rocks (blue colors indicate open pore spaces). B) The porosity that is present is

1214   predominantly secondary, mostly through grain dissolution of feldspars; this example shows remnant

1215   grain material preserved. C&D) Sample SK7F, interpreted as a hybrid bed. Thin section micrographs

1216   in plane polarized light (C) and with crossed polars (D). These images clearly show the abundant

1217   rock fragments which are common in all of the sampled rocks. Some fragments appear to be of

1218   carbonate rocks (I), although discrimination from altered plagioclase can be difficult, whilst others

1219   are composed of multiple minerals (II); calcite is recorded in the QEMSCAN mineralogical analysis

1220   for this sample.

1221   Figure 13. Summary diagrams illustrating grain-size trends, sorting, mineralogy and grain fabric for

1222   representative examples of hybrid beds (A, B, C) and one turbidite (D). Note that the straight lines

1223   between data points are for illustration only and do not indicate that data points can necessarily be

1224   extrapolated.

1225   Figure 14. Grain-size distribution curves for individual hybrid and turbidite beds. Whilst the grain

1226   size curves are largely distinctive for the different flow types (summarised in Fig. 15), SK2 although

1
2
3
4
5
6
7
8
9
10
11
12
13
14
15
16
17
18
19
20
21
22
23
24
25
26
27
28
29
30
31
32
33
34
35
36
37
38
39
40
41
42
43
44
45
46
47
48
49
50
51
52
53
54
55
56
57
58
59
60

1227 described as a hybrid bed has much the same character as a turbidite, albeit slightly enriched in

1228 coarser grains and with a more clay rich top (see Table 1).

1229 Figure 15. Representative grains-size distribution for deposits described as A) turbidites and B)

1230 hybrid beds. Turbidites are characterised by positively (fine) skewed lower bed divisions, and

1231 typically symmetrical upper divisions; in contrast, hybrid beds are characterised by negative (coarse)

1232 skewed lower divisions and symmetrical to coarse upper divisions.

1233 Figure 16. Flow parameters along lobe length for a scenario where channel width is 250 m; channel

1234 depth and initial flow thickness are 13 m and 17 m respectively; flow concentration is 5%; slope is

1235 $1.5*10^{-3}$; lobe width is 15 km; lobe length is 25km. (A) Flow width increases linearly over the lobe

1236 length from the channel width at the lobe apex to the full lobe width. Flow thickness decreases

1237 rapidly proximally, and more slowly distally. (B) Average velocity (left y-axis) and bed-shear

1238 velocity (right y-axis). Plots overlap because the drag coefficient has been used to normalise the

1239 right y-axis according to Eq. (4). (C) Suspension capacity parameter Γ is much larger than 1 at the

1240 lobe apex, indicating undersaturated near-bed conditions, reaches the threshold value of Γ =1 21 km

1241 downstream of the lobe apex, and Γ <1, leading to turbulence suppression, downstream of 21 km.

1242

1243 Figure 17. The sensitivity of the downstream evolution of Γ to different estimations for inlet

1244 concentration and slope. (A) Sediment concentrations of 10%, 5%, 1%, and 0.5%; for a given slope,

1245 the distance to flow transformation increases with increasing sediment concentration. (B) Slope

1246 gradients of $5.0*10^{-3}$, $2.5*10^{-3}$, $1.5*10^{-3}$, $1*10^{-3}$, and $5.0*10^{-4}$; for a given concentration, the distance

1247 to flow transformation increases with increasing slope.

1248 Figure 18. A) Schematic perspective/plan view of Fans 3. The distribution of hybrid beds is

1249 illustrated with schematic logs (see 'B'), but note that the fan fringe is not limited to hybrid beds,

1250 low-density turbidites are also common. At t0, in the trunk channels, flows are undersaturated with

1251 respect to the flow suspension capacity (Γ >1) and strongly erosional; high density turbidites are

1252 amalgamated and can be mudstone-clast rich. B) Summary diagram of flow evolution and deposit

1253 type for flows in the fringe area which start out, at t1, fully turbulent and well mixed and

1254 undersaturated (Γ >1), capable of eroding and entraining substrate. As flows decelerate from the

1255 channel-lobe transition (t2), shear stress exerted on the bed decreases, leaving substrate interaction

1256 preserved and resultant deposits clast and mud rich. Further deceleration and enrichment in cohesive

1257   and fine grained material (t3) results in the concentration profile becoming increasingly stratified

1258   and, when flows drop below the critical value of $\Gamma=1$ they are oversaturated and suspension capacity

1259   is lost. A dense lower layer forms, which continues to move downstream owing to its high water

1260   content (due to clays and very fine silts), grains are supported by yield strength but coarser grains

1261   settle resulting in a relatively well sorted sand fraction within a mud-rich matrix. Overlying layers

1262   are muddier and less well sorted. The formation of this high concentration lower boundary layer

1263   flow inhibits the transmission of turbulent kinetic energy into the upper part of the flow and

1264   turbulence is rapidly dissipated (t4).

1265

1266
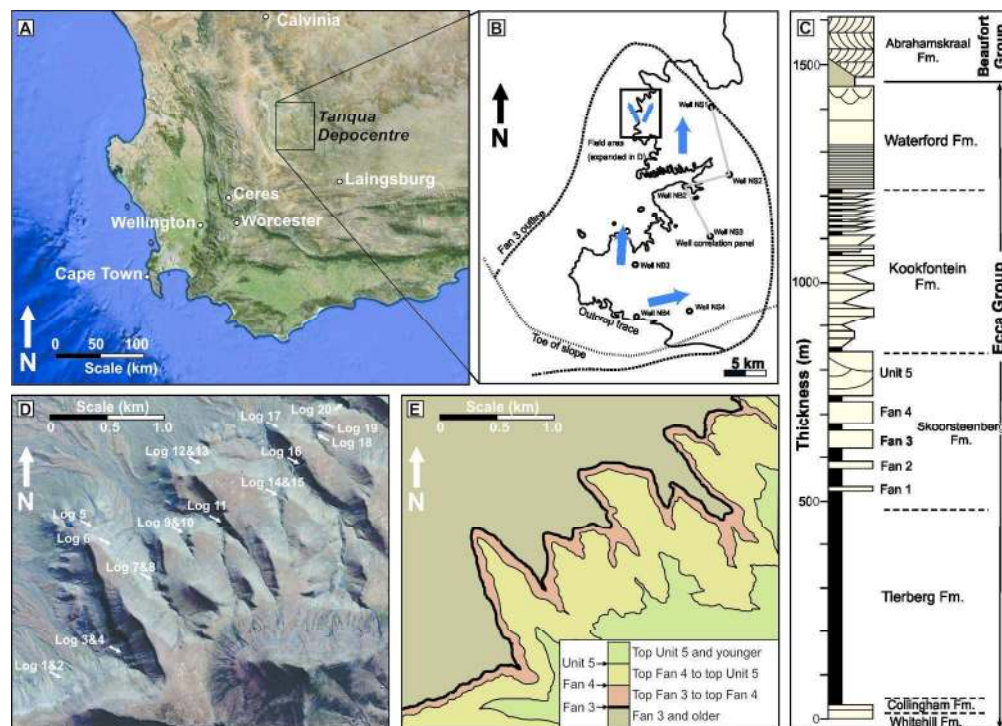
Figure 1. A) Aerial image of part of South Africa, highlighting the location of the Tanqua Depocentre, approximately 90 km northwest of the town of Laingsburg. B) Outline of Fan 3 in the Tanqua Depocentre (from Hodgson et al., 2006); the field area is boxed and expanded in 'D' and 'E'. Blue arrows show the general palaeoflow trends. C) Aerial image of the field area, illustrating the outcrop continuity of the near horizontal bedding surfaces, and the location of the measured sections. D) Schematic stratigraphic log of the Permian to earliest Triassic deep-marine to fluvial fill of the Tanqua depocentre (modified from Wild et al., 2005). E) Simple geological map illustrating the position of Fan 3 (bold line) and stratigraphic packages between fan tops. At this scale the fan tops are the only mappable surfaces, as the fans tend to weather into steep outcrop faces, whereas the finer-grained inter-fans form gentler slopes. The sandy part of Fan 2 has pinched out in this area (pinching out to the north), and is beneath the resolution of this map; Fan 1 has pinched out. The uppermost package, i.e., 'Top Unit 5 and younger', is predominantly the Kookfontein Fm.

170x123mm (300 x 300 DPI)
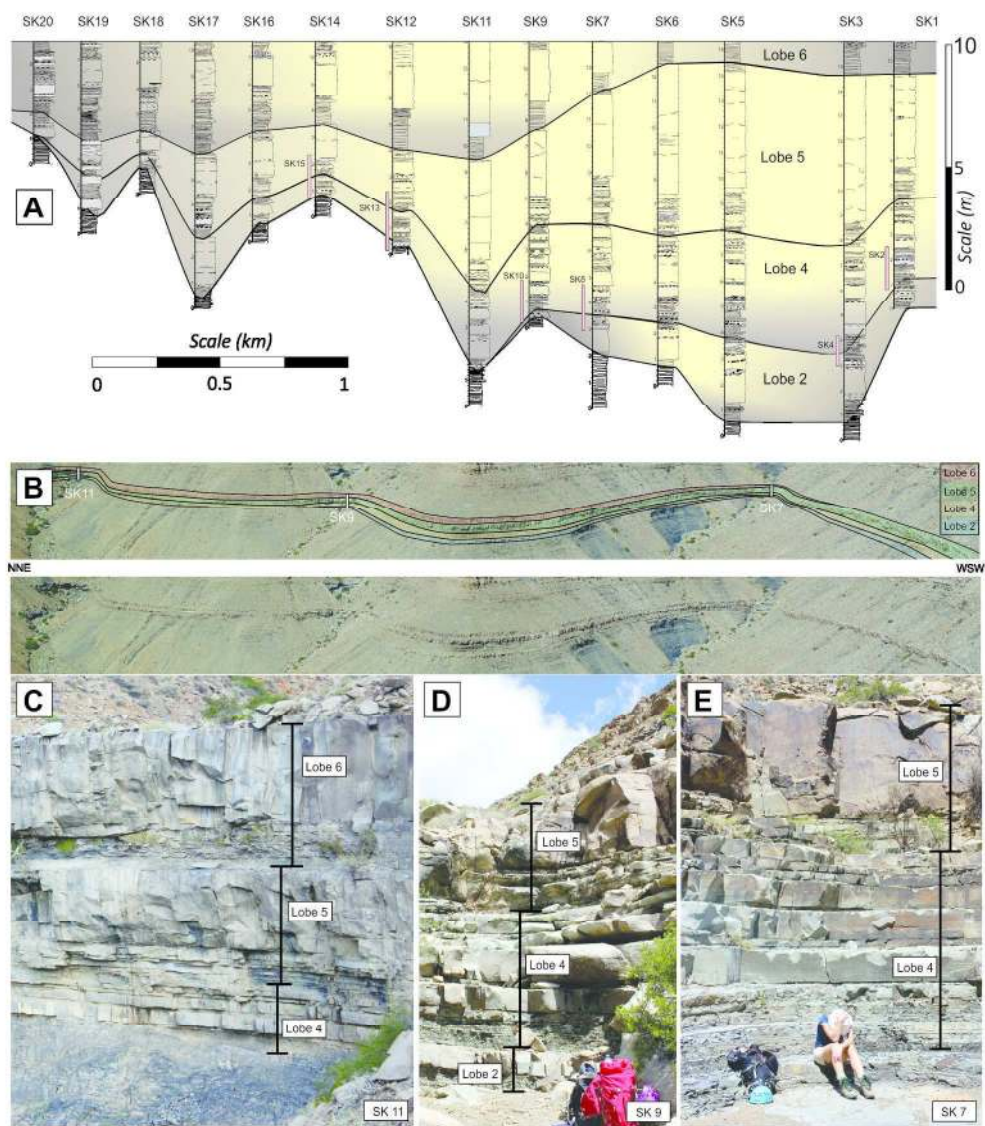
Figure 2. A) Correlation panel of 1:20 outcrop logs SK1-20; positions of 1:2 logs are shown alongside the relevant log. The correlations are based on walking out key stratigraphic surfaces, the lobes stack to form a lobe complex (Fan 3). Note that lobes 1 and 3 have pinched out in this position. The outcrop panel (B) shows the general character and exposure of the distal parts of Fan 3. C, D and E illustrate the general outcrop character at the positions of logs SK11, SK9 and SK7 respectively. The yellow and grey colouring gives a general indication of the sandstone (yellow) and mudstone (grey) distribution. Palaeoflow is to the north, approximately right to left in the image.

196x223mm (300 x 300 DPI)

Figure 3. (A) Correlation panel of logged sections from behind outcrop boreholes, spanning Fan 3 from the proximal channel-dominated part (Ongeluks River outcrops), to the channel-lobe transition and across the lobe to the distal parts studied here (e.g., Boreholes NB2-NS1). Note that the environments indicated are at the point of the arrows, not spanning the entire fan at that location. Correlations are tentative owing to the complex nature of compensational lobe stacking patterns and based on finer-grained intervals subdividing the sandstone rich element, following Prélat et al., 2009. A clear facies trend is observed across the lobe complex, illustrated by the plan view image (B).

170x197mm (300 x 300 DPI)
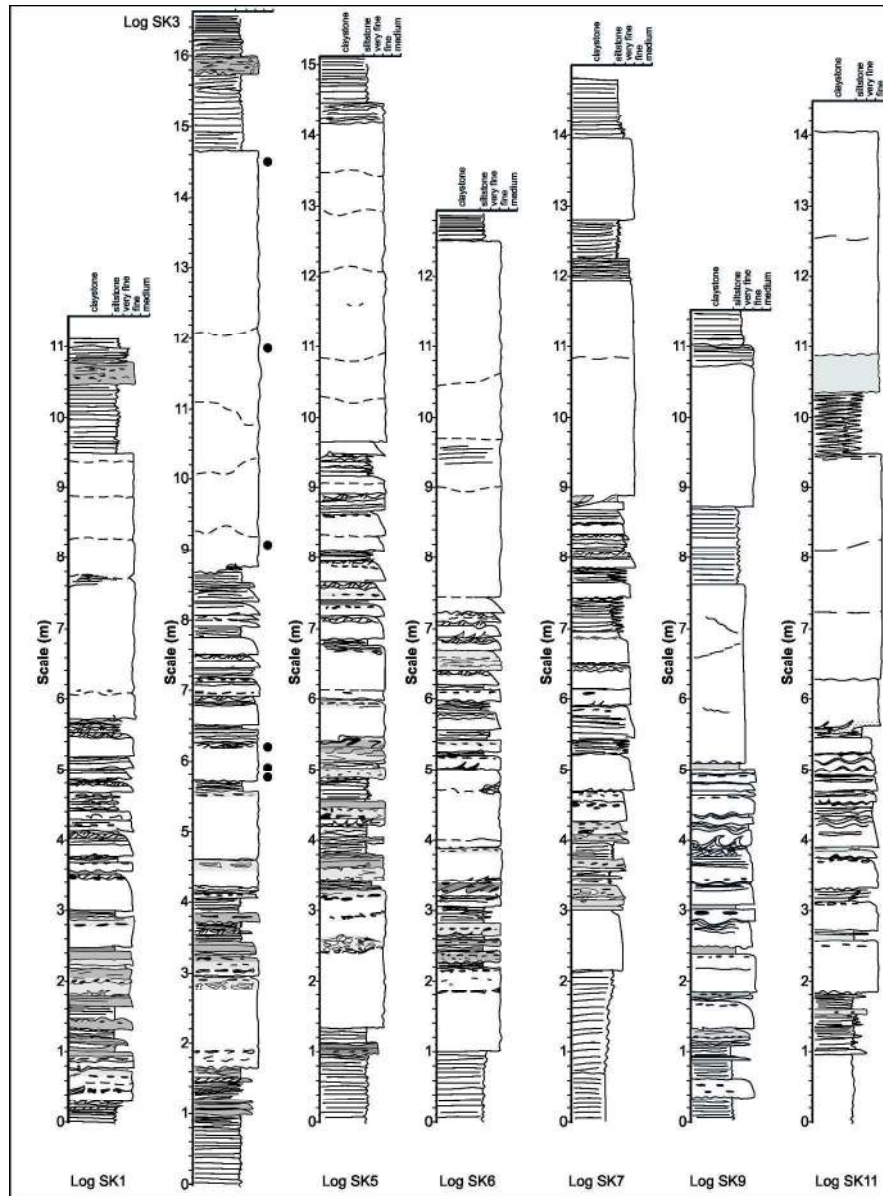
Figure 4. Sedimentary logs through Fan 3, positions shown in Figure 1.

173x231mm (300 x 300 DPI)

1
2
3
4
5
6
7
8
9
10
11
12
13
14
15
16
17
18
19
20
21
22
23
24
25
26
27
28
29
30
31
32
33
34
35
36
37
38
39
40
41
42
43
44
45
46
47
48
49
50
51
52
53
54
55
56
57
58
59
60
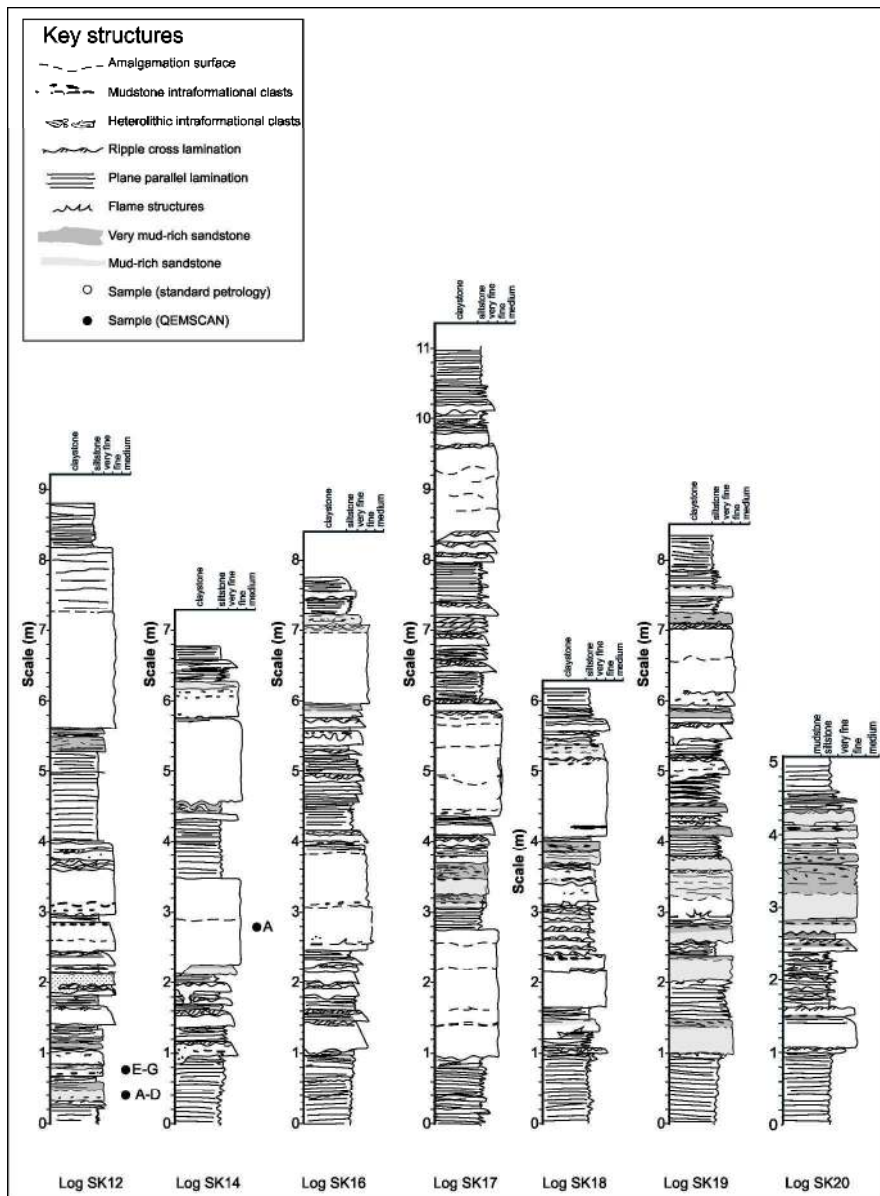
Figure 4. Sedimentary logs through Fan 3, positions shown in Figure 1.
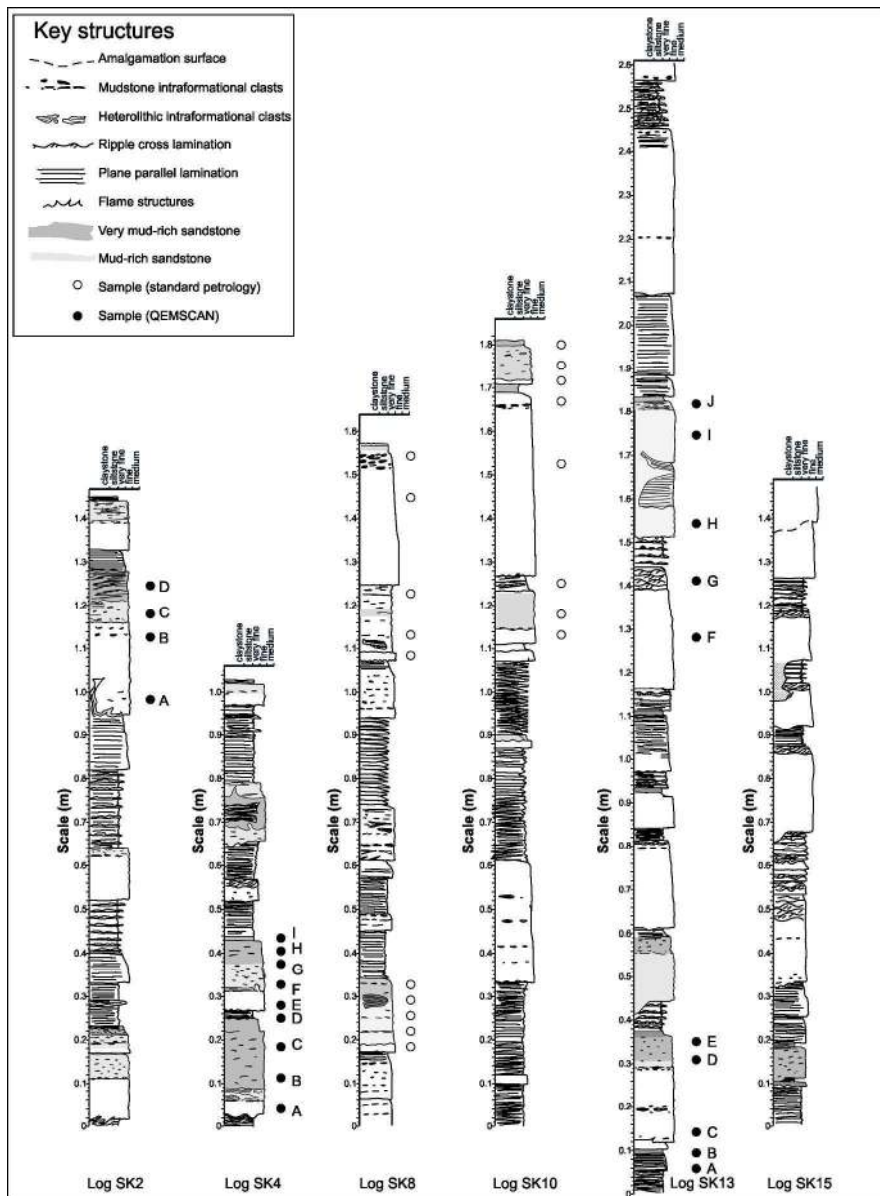
170x231mm (300 x 300 DPI)

Figure 5. Detailed sedimentary logs from Fan 3, positions shown in Figure 1.

170x231mm (300 x 300 DPI)
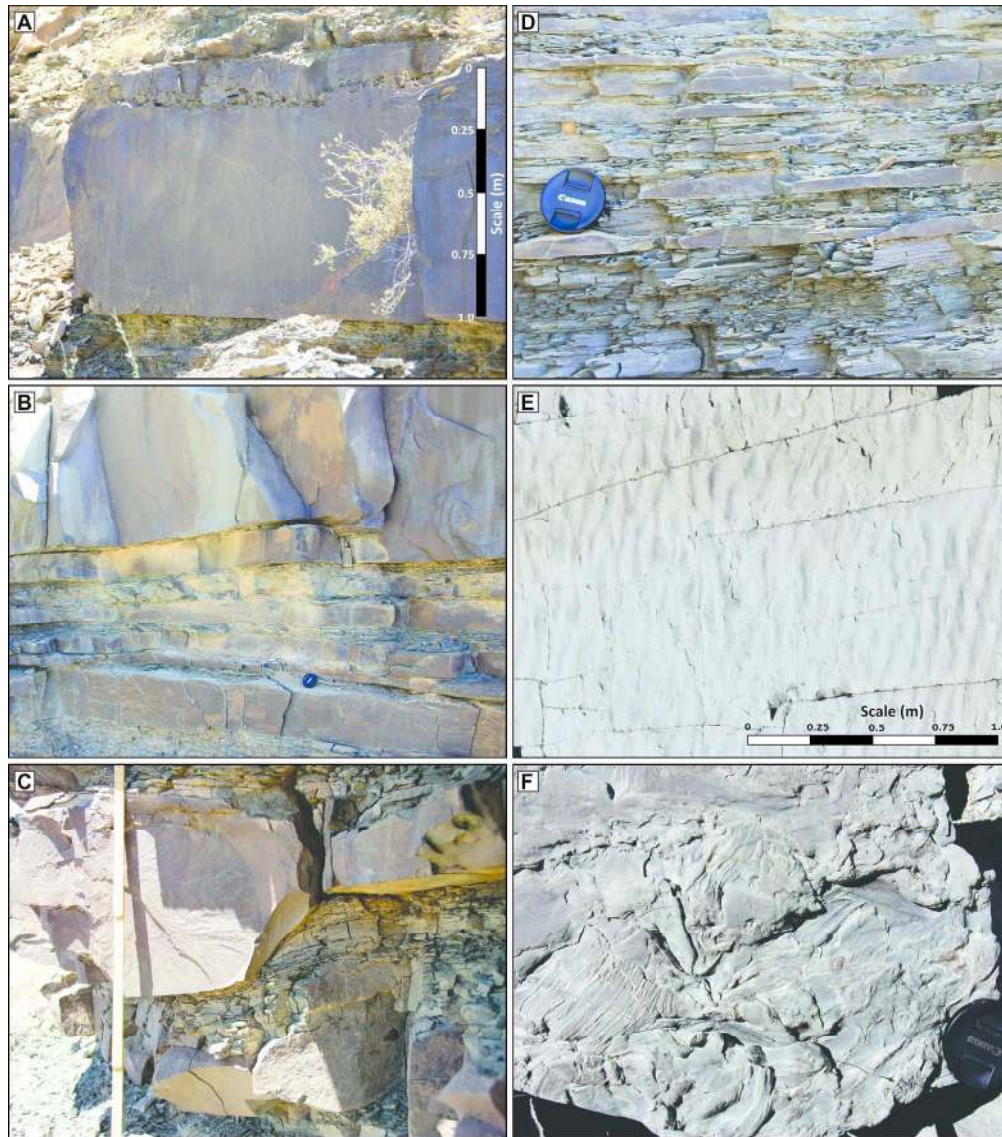
Fig. 6. Representative turbidite facies. A) Thick bedded turbidite with a sharp base, weak normal grading and with a clast-rich upper part; clasts are partly disaggregated generating clay-rich patches within the sandstone. B) Erosional bed bases typically plane out on mudstones and cut downwards in a stepwise manner through thin-bedded intervals, occasionally with contemporaneous lateral injection. C) Erosional step at base of medium-bedded sandstone which is loaded into underlying thin-bedded silty turbidites. D) Thin-bedded very-fine-grained low-density turbidites. E) Rippled bed top to low density turbidite. F) Plant imprints in an intra-bed division.

170x192mm (300 x 300 DPI)
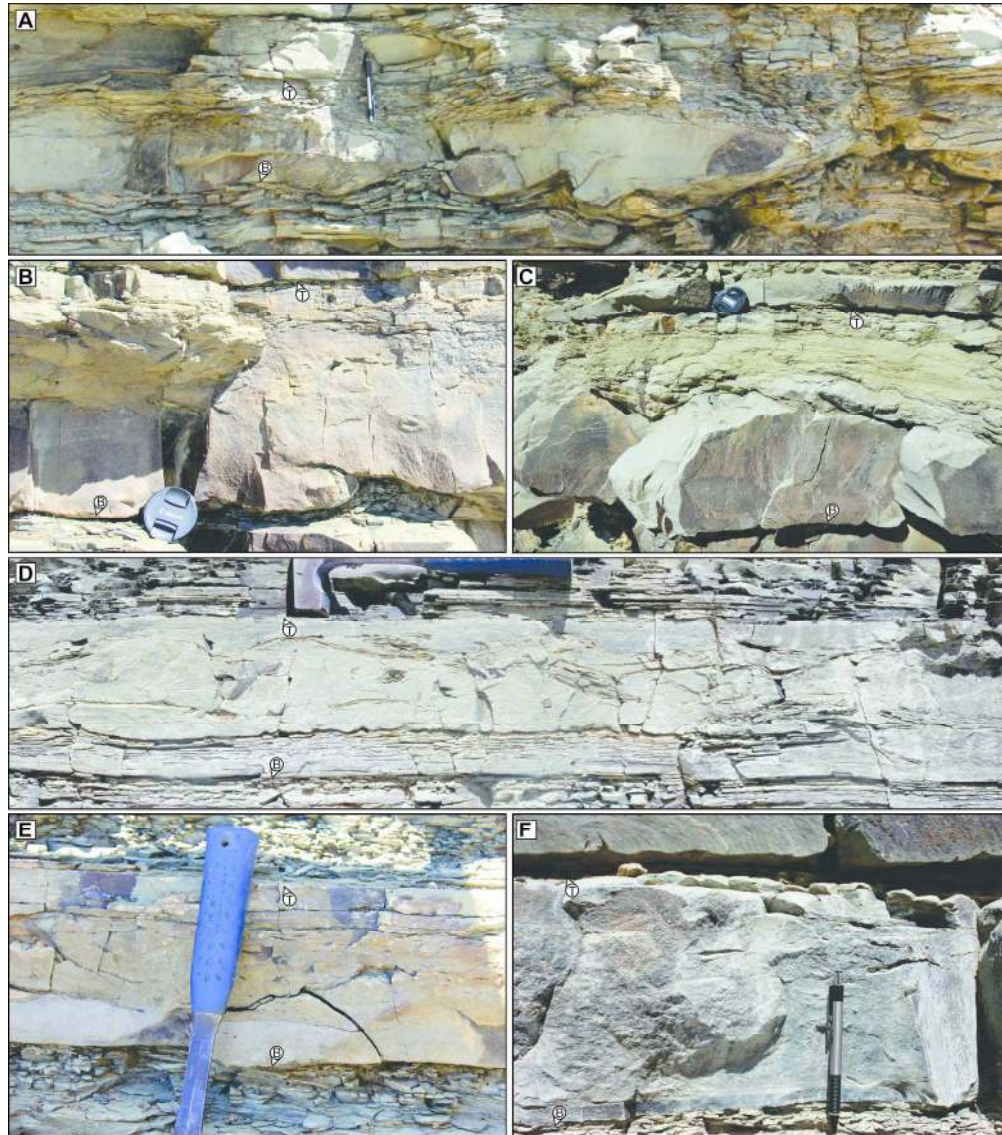
Fig. 7. Representative hybrid bed photographs ('B' and 'T' symbols indicate base and top of beds). A) Bed showing intense interaction with the substrate and muddy upper part, these are typical in medial lobe settings. B & C) Hybrid beds with thick laminar/ high concentration flow deposits in their upper parts; these are typical in medial to distal settings. D) Hybrid beds with large rafts of siltstone and mudstone. E & F) Thin hybrid beds characteristic of the distal facies, with thin relatively clean sands at bed bases and overlying layers of varying mud content.

170x192mm (300 x 300 DPI)
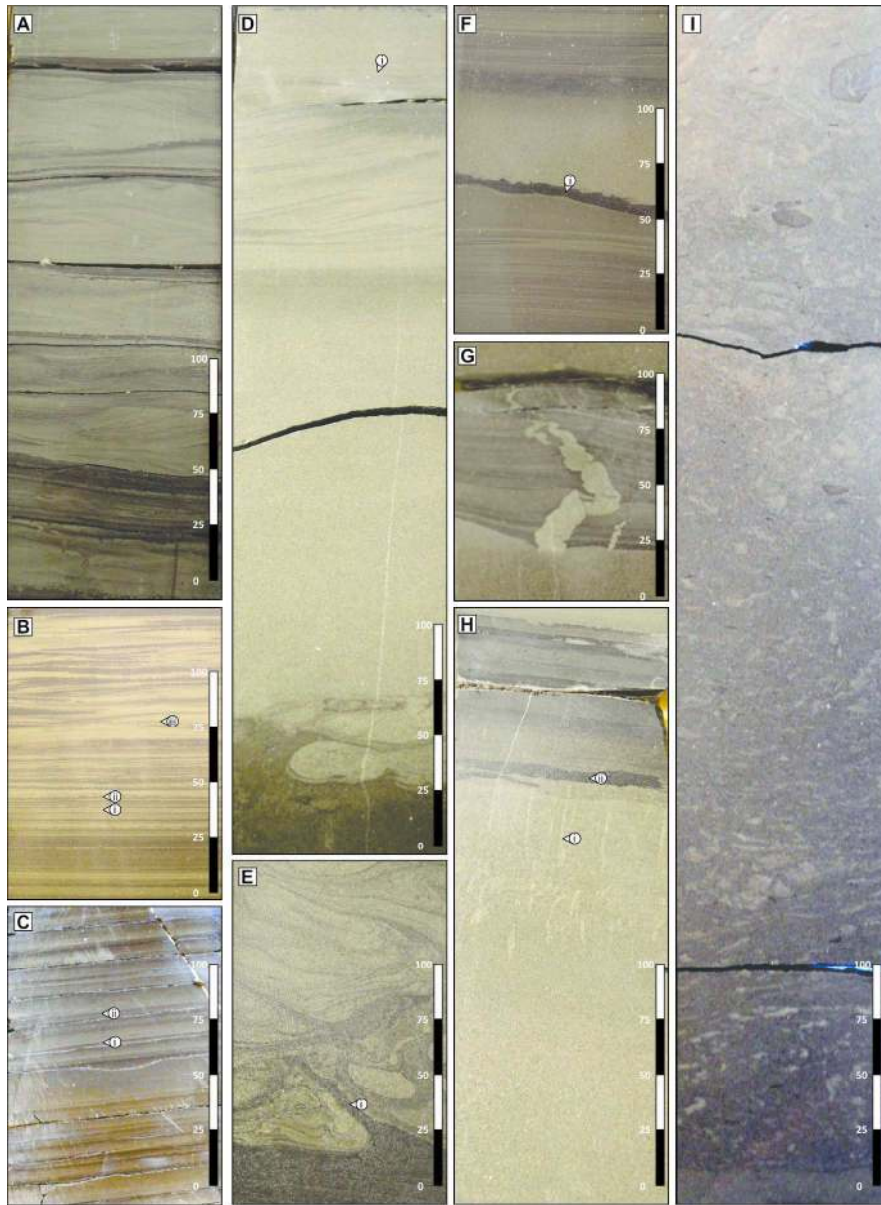
Figure 8. Photographs from cores of representative facies. A) Thin-bedded low-density turbidites; B) Thinly-interbedded low-density turbidites dominated by planar-lamination (i), small-scale load and flame structures (ii), and ripple-cross lamination (iii). C) Silty low-density turbidites graded from medium silt (i) to very-fine silt (ii). D) Turbidite with loading and injection of the substrate at the base. The upper part of the bed is truncated (i). E) Detail of loading and deformation at the base of a turbidite. F) Muddy sandstone truncated by an erosion surface overlain by claystone (bypass surface) and overlain by an argillaceous sandstone. G) Small injectite extending from a bed top. H) Dewatering pillars in the upper part of a hybrid bed, (ii) large mudstone clasts. I) Thick debrite with cleaner sandstone 'balls' and injections in an overall muddy sand matrix.

169x229mm (300 x 300 DPI)
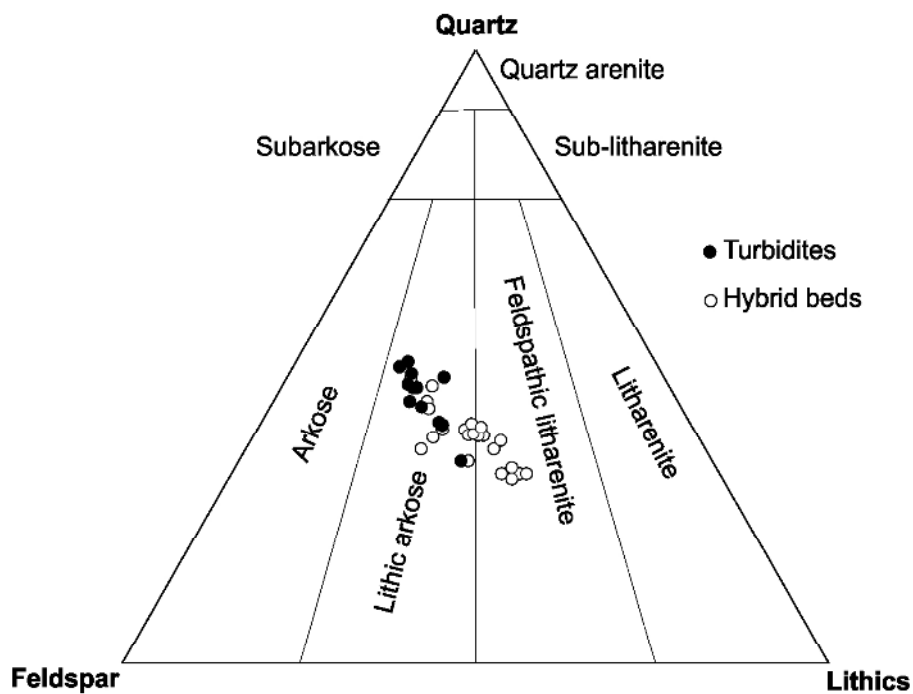
Fig. 9. Quartz-feldspar-lithics (QFL) plot for samples subdivided into 'turbidites' and 'hybrid beds. Turbidites fall entirely within the lithic arkose class, whilst hybrid beds span the lithic arkose and feldspathic litharenite classes. Ternary plot from Folk (1974).

149x110mm (300 x 300 DPI)
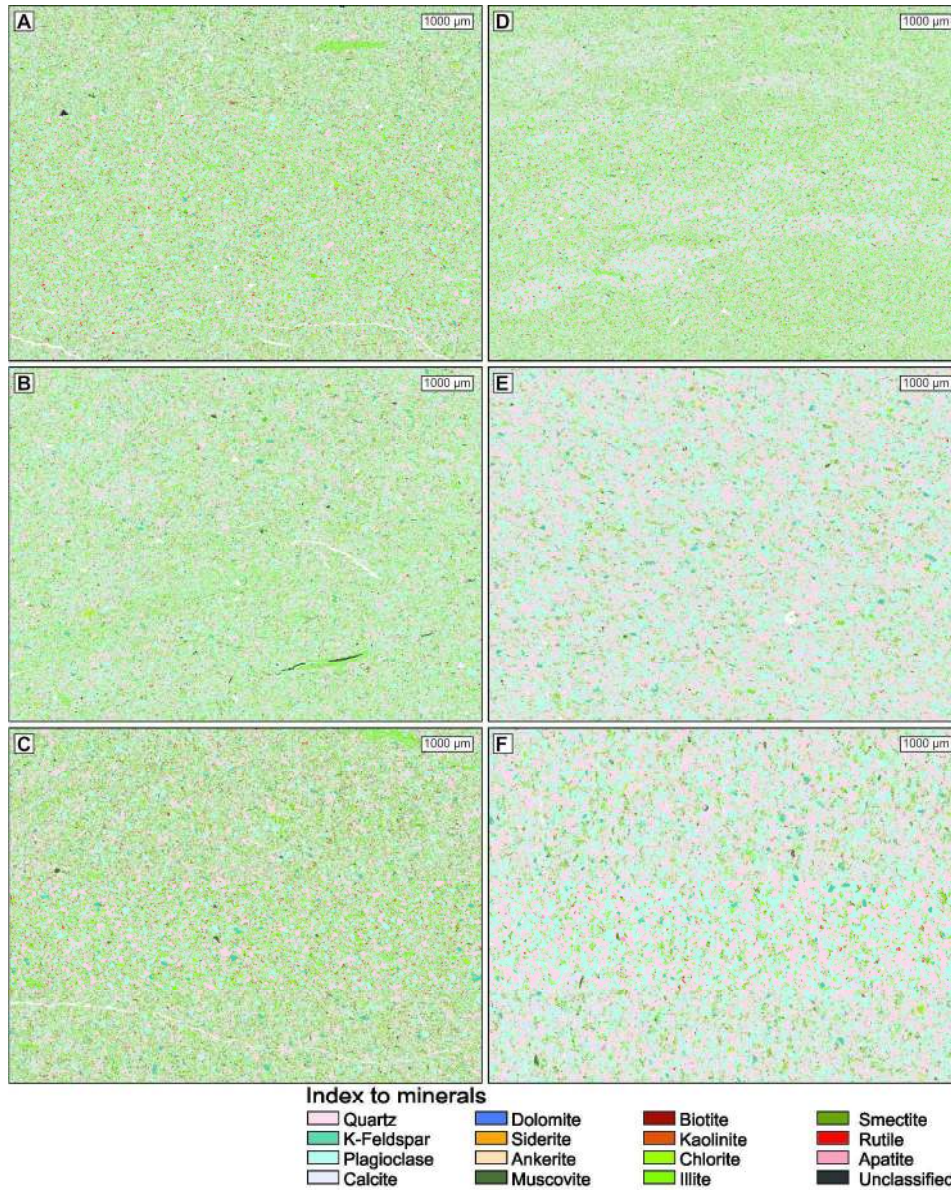
Figure 10. Mineral maps from thin-sections, based on chemical composition data from QEMSCAN. A-F show samples SK7A, B, C, D, H and I respectively. SK7A-D are interpreted as hybrid beds whilst SK7H and SK7I are interpreted as turbidites (see table 1).

170x214mm (300 x 300 DPI)
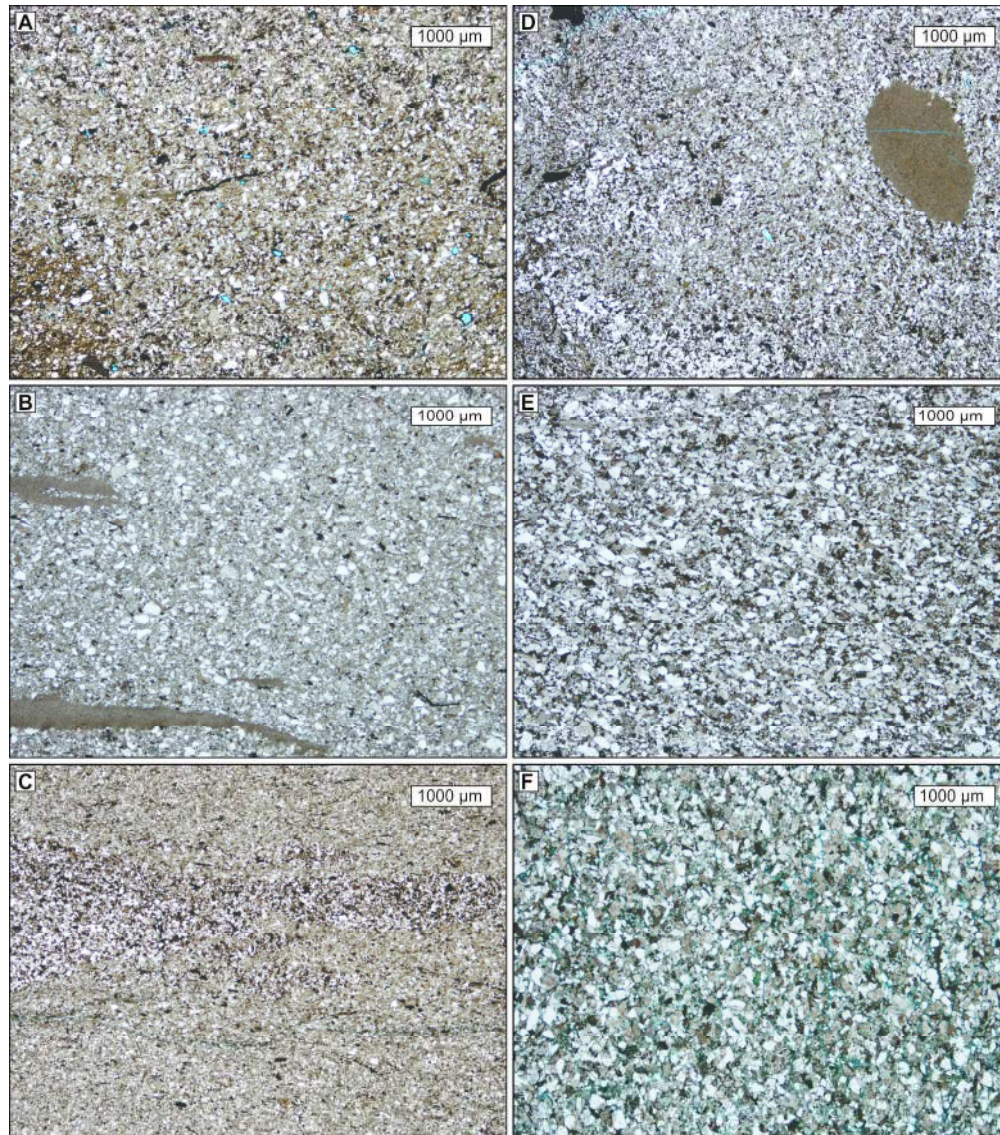
Figure 11. Representative thin-section photomicrographs. A) Sample SK7B: clay-rich sample from the middle part of a hybrid bed. Note the organic fragments and porosity (blue) due to dissolution of framework minerals (probably feldspar). B) Sample SK7C: from the middle division of a hybrid bed, this clay-rich sandstone has a strong bed-parallel grain fabric, with aligned claystone and organic clasts. C) Sample SK7D: Sample from a thick muddy division within a hybrid bed, note the strong grain fabric with lens of coarser-grained sediment in the centre of the image. The sample lacks visible porosity. D) Sample SK7E: Mixed 'swirled' fabric of relatively finer- and coarser-grained lenses. This sample is from a lighter coloured band in a hybrid bed. The large rounded clast is a claystone. Note the porosity due to grain dissolution. E) Sample SK7H: This sample is from a tractional sandstone with weak plane-parallel lamination, which has a much lower mud content than the previous examples, and an alignment of quartz and feldspar grains along laminae. F) Sample SH7I. This sample is from the very-thick bed which caps Fan 3 at the SK7 locality. It does not appear to have a strong grain fabric in thin-section and in outcrop lacks obvious tractional structure. The visible porosity is most-likely related to weathering processes and fracturing around coarser grains.

170x192mm (300 x 300 DPI)

1
2
3
4
5
6
7
8
9
10
11
12
13
14
15
16
17
18
19
20
21
22
23
24
25
26
27
28
29
30
31
32
33
34
35
36
37
38
39
40
41
42
43
44
45
46
47
48
49
50
51
52
53
54
55
56
57
58
59
60
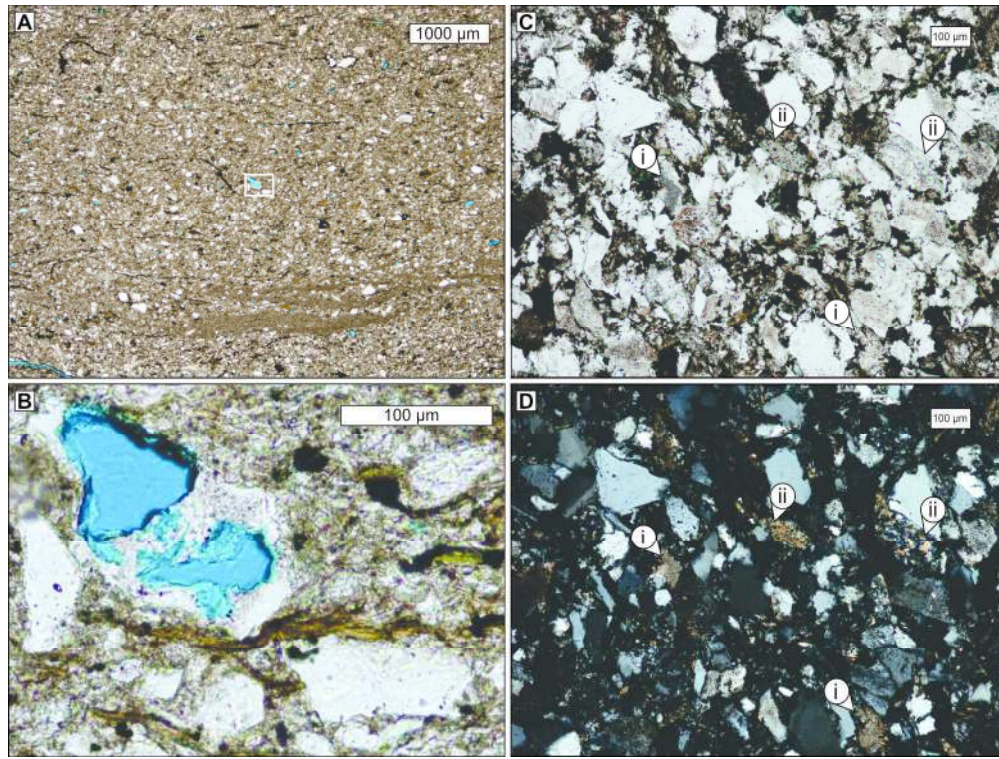
Figure 12. Thin-section photomicrographs in plane polarized light, from an argillaceous sandstone division of a hybrid bed (Sample SK7A, Log SK7. A) Illustration of the very low degree of porosity in these rocks (blue colors indicate open pore spaces). B) The porosity that is present is predominantly secondary, mostly through grain dissolution of feldspars; this example shows remnant grain material preserved. C&D) Sample SK7F, interpreted as a hybrid bed. Thin section micrographs in plane polarized light (C) and with crossed polars (D). These images clearly show the abundant rock fragments which are common in all of the sampled rocks. Some fragments appear to be of carbonate rocks (I), although discrimination from altered plagioclase can be difficult, whilst others are composed of multiple minerals (II); calcite is recorded in the QEMSCAN mineralogical analysis for this sample.

170x128mm (300 x 300 DPI)

1
2
3
4
5
6
7
8
9
10
11
12
13
14
15
16
17
18
19
20
21
22
23
24
25
26
27
28
29
30
31
32
33
34
35
36
37
38
39
40
41
42
43
44
45
46
47
48
49
50
51
52
53
54
55
56
57
58
59
60

Figure 13. Summary diagrams illustrating grain-size trends, sorting, mineralogy and grain fabric for representative examples of hybrid beds (A, B, C) and one turbidite (D). Note that the straight lines between data points are for illustration only and do not indicate that data points can necessarily be extrapolated.

170x184mm (300 x 300 DPI)

Figure 13. Summary diagrams illustrating grain size trends, sorting, mineralogy and grain fabric for representative examples of hybrid beds (A, B, C) and one turbidite (D). Note that the straight lines between data points are for illustration only and do not indicate that data points can necessarily be extrapolated.

170x184mm (300 x 300 DPI)

Figure 14. Grain size distribution curves for individual hybrid and turbidite beds. Whilst the grain size curves are largely distinctive for the different flow types (summarised in Fig. 15), SK2 although described as a hybrid bed has much the same character as a turbidite, albeit slightly enriched in coarser grains and with a more clay rich top (see Table 1).

167x167mm (300 x 300 DPI)
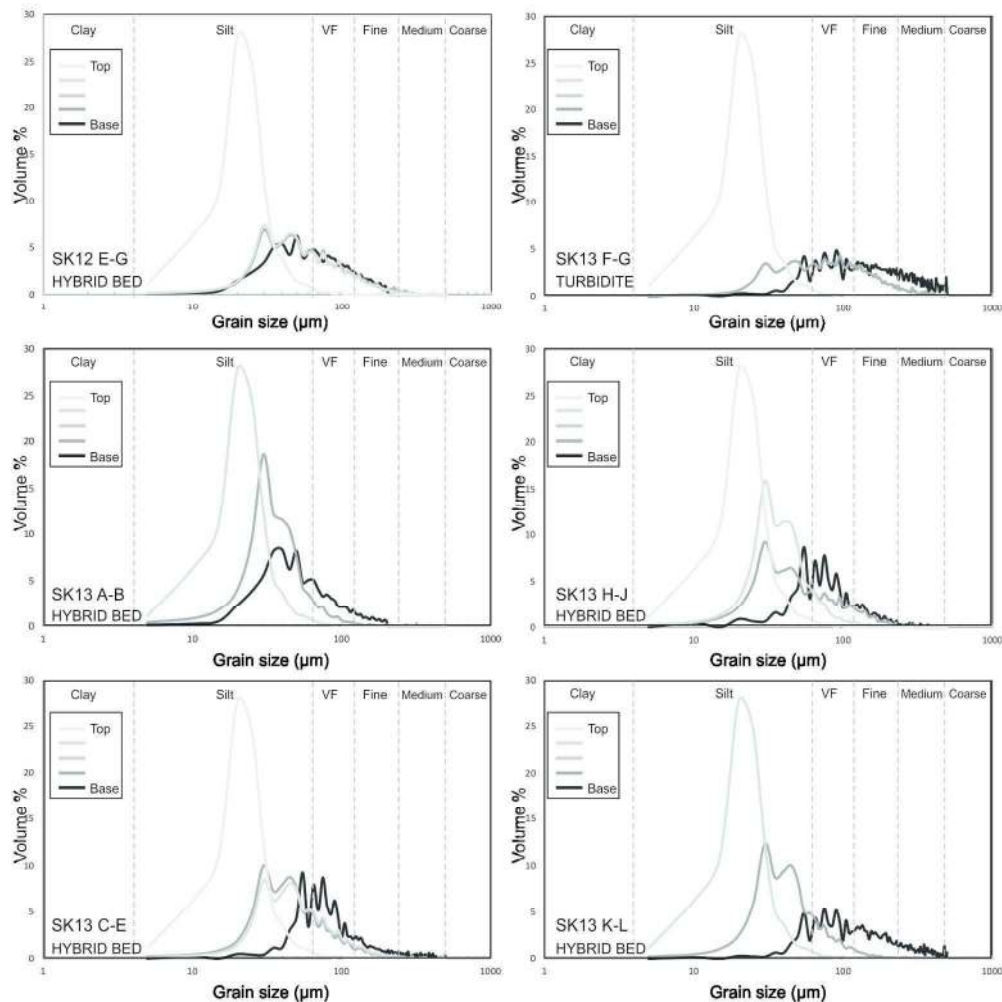
Figure 15. Representative grains-size distribution for deposits described as A) turbidites and B) hybrid beds. Turbidites are characterised by positively (fine) skewed lower bed divisions, and typically symmetrical upper divisions; in contrast, hybrid beds are characterised by negative (coarse) skewed lower divisions and symmetrical to coarse upper divisions.

167x167mm (300 x 300 DPI)

1
2
3
4
5
6
7
8
9
10
11
12
13
14
15
16
17
18
19
20
21
22
23
24
25
26
27
28
29
30
31
32
33
34
35
36
37
38
39
40
41
42
43
44
45
46
47
48
49
50
51
52
53
54
55
56
57
58
59
60
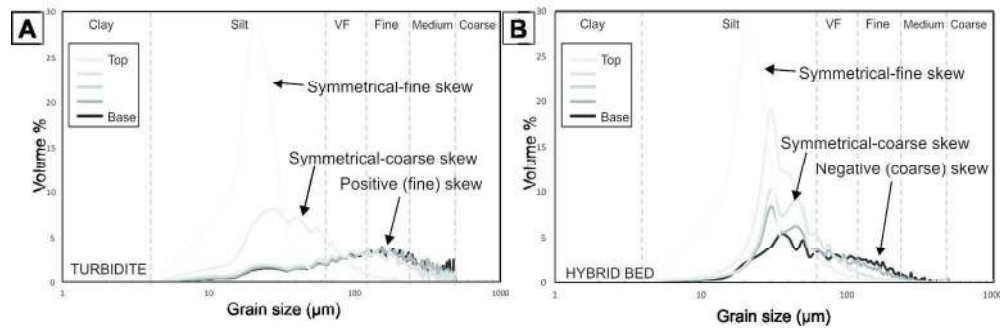
Figure 15. Representative grains size distributions for deposits described as A) turbidites and B) hybrid beds. Turbidites are characterized by positively (fine) skewed lower bed divisions, and typically symmetrical upper divisions; in contrast, hybrid beds are characterized by negative (coarse) skewed lower divisions and symmetrical to coarse upper divisions.

171x56mm (300 x 300 DPI)
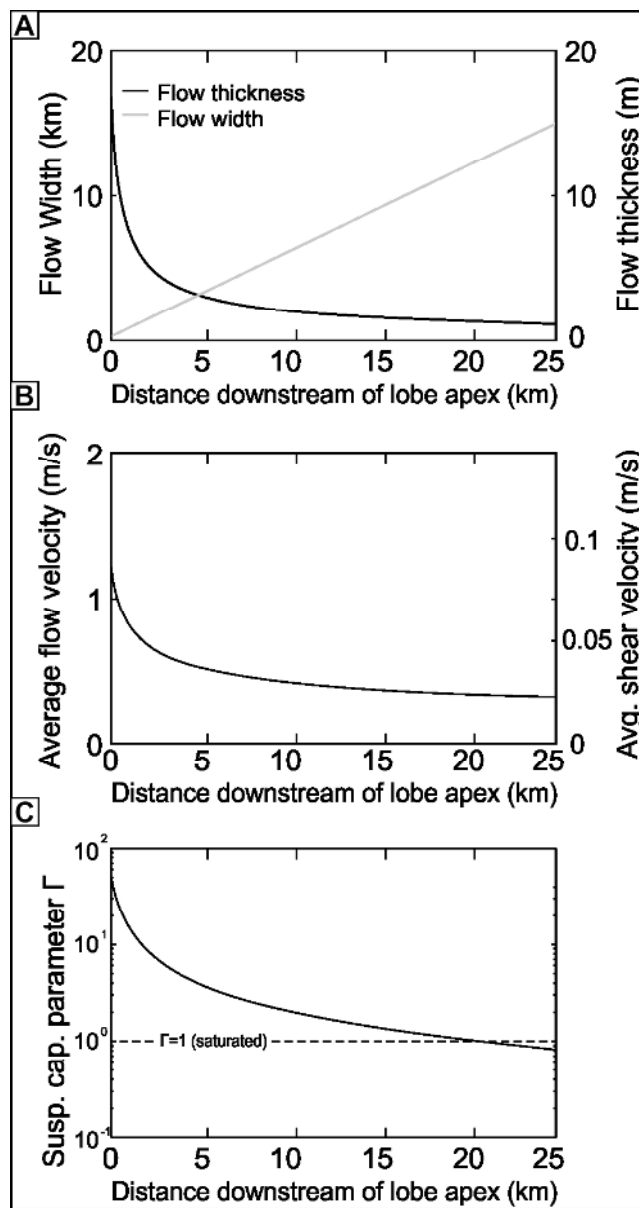
Figure 16. Flow parameters along lobe length for a scenario where channel width is 250 m; channel depth and initial flow thickness are 13 m and 17 m respectively; flow concentration is 5%; slope is 1.5*10-3; lobe width is 15 km; lobe length is 25km. (A) Flow width increases linearly over the lobe length from the channel width at the lobe apex to the full lobe width. Flow thickness decreases rapidly proximally, and more slowly distally. (B) Average velocity (left y-axis) and bed-shear velocity (right y-axis). Plots overlap because the drag coefficient has been used to normalise the right y-axis according to Eq. (4). (C) Suspension capacity parameter Γ is much larger than 1 at the lobe apex, indicating undersaturated near-bed conditions, reaches the threshold value of Γ =1 21 km downstream of the lobe apex, and Γ <1, leading to turbulence suppression, downstream of 21 km.

80x150mm (300 x 300 DPI)
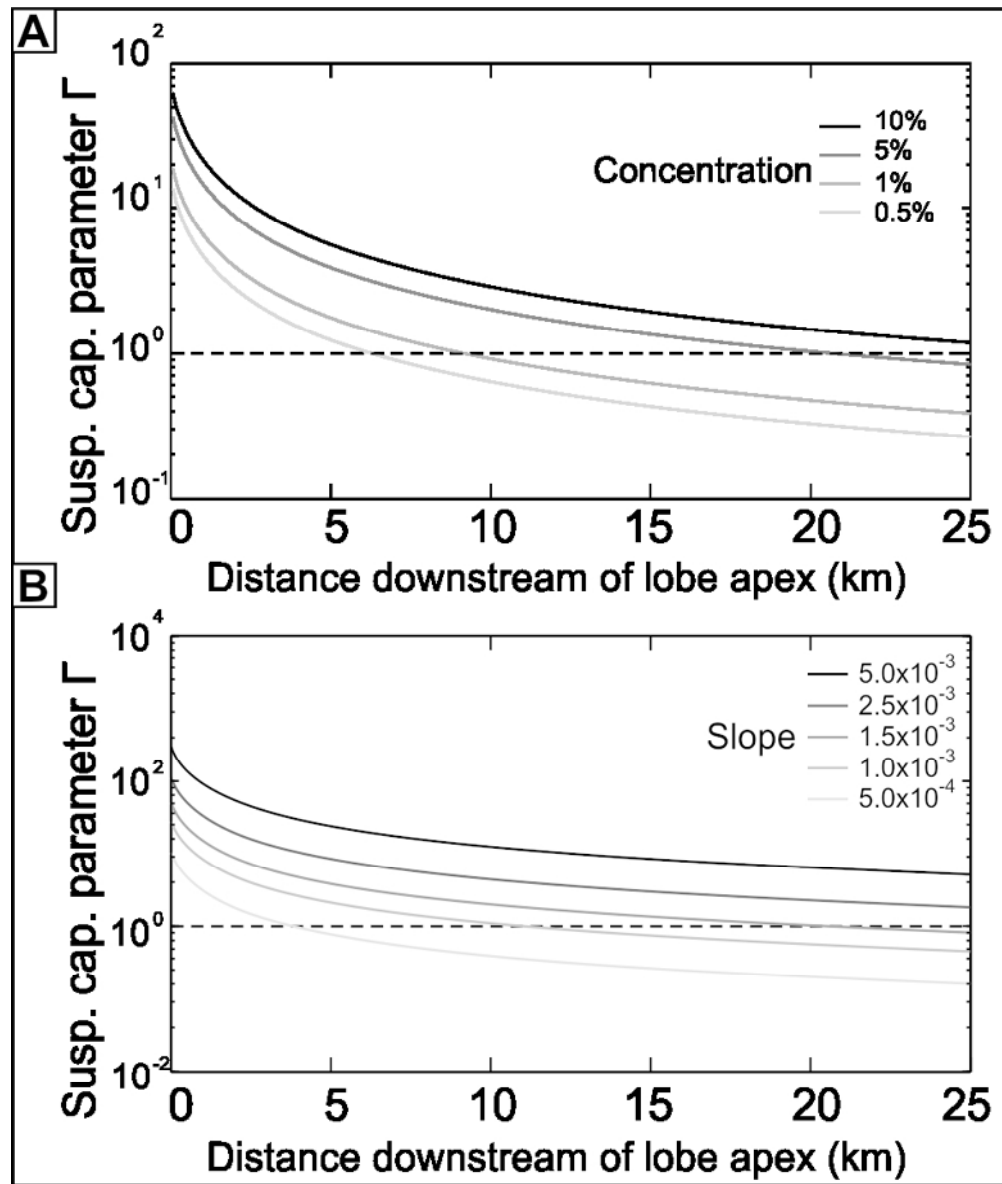
1
2
3
4
5
6
7
8
9
10
11
12
13
14
15
16
17
18
19
20
21
22
23
24
25
26
27
28
29
30
31
32
33
34
35
36
37
38
39
40
41
42
43
44
45
46
47
48
49
50
51
52
53
54
55
56
57
58
59
60

Figure 17. The sensitivity of the downstream evolution of Γ to different estimations for inlet concentration and slope. (A) Sediment concentrations of 10%, 5%, 1%, and 0.5%; for a given slope, the distance to flow transformation increases with increasing sediment concentration. (B) Slope gradients of 5.0*10-3, 2.5*10-3, 1.5*10-3, 1*10-3, and 5.0*10-4; for a given concentration, the distance to flow transformation increases with increasing slope.

80x94mm (300 x 300 DPI)
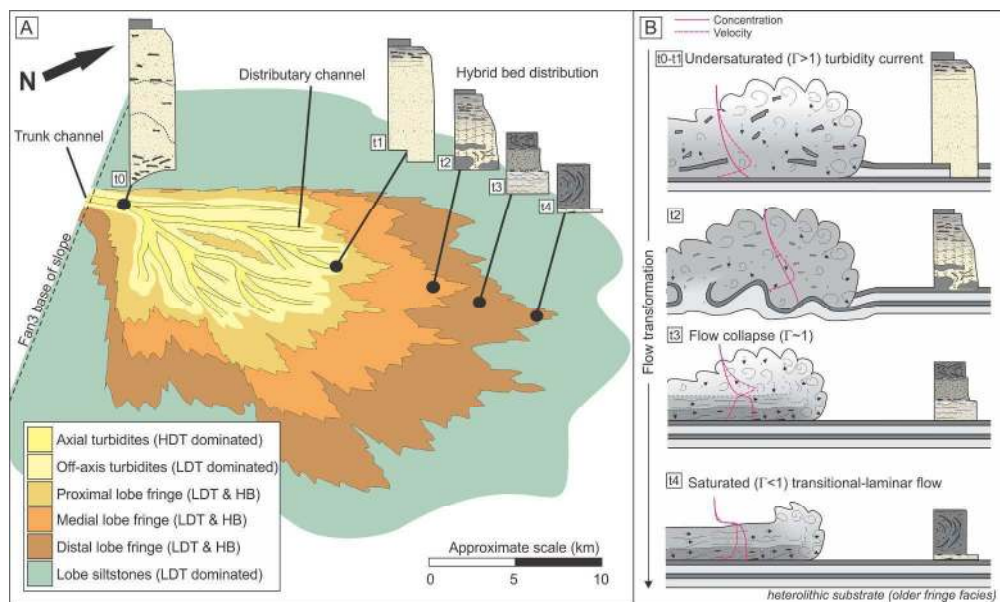
Figure 18. A) Schematic perspective/plan view of Fans 3. The distribution of hybrid beds is illustrated with schematic logs (see 'B'), but note that the fan fringe is not limited to hybrid beds, low-density turbidites are also common. At t0, in the trunk channels, flows are undersaturated with respect to the flow suspension capacity ($\Gamma >1$) and strongly erosional; high density turbidites are amalgamated and can be mudstone-clast rich. B) Summary diagram of flow evolution and deposit type for flows in the fringe area which start out, at t1, fully turbulent and well mixed and undersaturated ($\Gamma >1$), capable of eroding and entraining substrate. As flows decelerate from the channel-lobe transition (t2), shear stress exerted on the bed decreases, leaving substrate interaction preserved and resultant deposits clast and mud rich. Further deceleration and enrichment in cohesive and fine grained material (t3) results in the concentration profile becoming increasingly stratified and, when flows drop below the critical value of $\Gamma=1$ they are oversaturated and suspension capacity is lost. A dense lower layer forms, which continues to move downstream owing to its high water content (due to clays and very fine silts), grains are supported by yield strength but coarser grains settle resulting in a relatively well sorted sand fraction within a mud-rich matrix. Overlying layers are muddier and less well sorted. The formation of this high concentration lower boundary layer flow inhibits the transmission of turbulent kinetic energy into the upper part of the flow and turbulence is rapidly dissipated (t4).

223x132mm (300 x 300 DPI)

Id	SK2A	SK2B	SK2C	SK2D	SK3A	SK3B	SK3C	SK3D	SK3E	SK3F	SK4A	SK4B	SK4C	SK4D	SK4E	SK4F	SK4G	SK4H	SK4I
Bed Type	HB-base	HB	HB	HB-top	TURB-base	TURB	TURB-top	AMAL-base	AMAL	AMAL-top	HB-base	HB	HB	HB-top	HB-base	HB	HB	HB	HB-top
Mineral Mass (%)																			
Quartz	46.25	44.95	41.64	31.86	46.07	47.38	38.76	44.48	42.99	42.77	38.08	32.08	37.00	30.67	41.96	34.79	37.51	36.27	30.18
Plagioclase	34.87	35.53	33.42	28.82	35.49	35.47	33.12	33.32	34.80	34.74	32.73	28.36	31.88	24.83	32.38	28.37	30.81	29.93	25.15
K-Feldspar	2.00	1.89	1.97	2.01	1.91	1.81	1.80	2.05	1.72	2.16	2.40	2.11	2.54	1.30	2.37	1.80	1.80	1.94	1.34
Muscovite	1.01	0.96	0.98	1.82	0.90	1.00	1.45	1.02	1.03	1.02	1.35	1.87	1.35	1.73	1.18	1.52	1.52	1.58	1.63
Illite	9.02	9.78	12.81	22.28	8.67	8.30	15.31	9.42	8.83	9.84	15.79	25.69	17.36	32.89	12.93	24.55	18.24	19.52	31.98
Chlorite	3.78	3.25	5.15	8.03	3.71	3.41	6.05	6.68	6.26	4.46	5.31	5.21	5.92	4.40	4.74	4.54	5.94	6.44	5.22
Other clays	0.81	1.34	1.27	1.84	1.11	0.81	1.40	1.10	0.87	0.76	2.07	1.69	1.58	1.50	1.86	1.75	1.61	1.73	1.99
Calcite	0.11	0.10	0.29	0.13	0.00	0.00	0.00	0.00	1.76	2.38	0.00	0.00	0.00	0.00	0.00	0.00	0.00	0.00	0.02
Rutile	0.99	0.88	0.95	1.71	0.82	0.75	0.91	0.76	0.76	0.82	0.98	1.51	0.96	1.06	0.92	1.17	1.15	1.20	0.88
Apatite	0.39	0.33	0.37	0.58	0.44	0.42	0.51	0.40	0.35	0.33	0.45	0.55	0.47	0.67	0.46	0.53	0.55	0.55	0.62
Zircon	0.05	0.02	0.02	0.02	0.06	0.04	0.03	0.07	0.07	0.02	0.02	0.03	0.02	0.02	0.03	0.02	0.02	0.03	0.01
Others	0.01	0.04	0.02	0.02	0.27	0.03	0.03	0.02	0.02	0.01	0.02	0.02	0.04	0.05	0.06	0.02	0.01	0.01	0.09
Unclassified	0.71	0.94	0.90	0.89	0.57	0.56	0.63	0.68	0.54	0.67	0.81	0.89	0.88	0.90	1.12	0.84	0.83	0.80	0.96
Mineral Volume (%)																			
Quartz	46.71	45.42	42.35	32.56	46.56	47.79	39.33	44.93	43.42	43.21	38.66	32.79	37.56	31.39	42.52	35.48	38.14	36.92	30.87
Plagioclase	35.28	35.97	33.90	29.51	35.93	35.84	33.65	33.72	35.21	35.16	33.30	29.03	32.42	25.46	32.88	28.99	31.39	30.53	25.77
K-Feldspar	2.07	1.96	2.04	2.11	1.98	1.88	1.87	2.12	1.79	2.24	2.50	2.21	2.64	1.36	2.46	1.89	1.87	2.02	1.41
Muscovite	0.95	0.90	0.92	1.73	0.84	0.94	1.37	0.96	0.97	0.96	1.29	1.77	1.28	1.64	1.11	1.44	1.44	1.49	1.56
Illite	8.70	9.43	12.38	21.73	8.36	7.99	14.82	9.08	8.51	9.49	15.30	25.06	16.83	32.14	12.51	23.90	17.70	18.97	31.23
Chlorite	3.78	3.25	5.17	8.12	3.71	3.41	6.07	6.68	6.26	4.46	5.34	5.28	5.95	4.46	4.76	4.69	5.99	6.49	5.29
Other clays	0.73	1.18	1.13	1.64	0.98	0.73	1.24	0.97	0.77	0.67	1.82	1.53	1.41	1.36	1.65	1.58	1.43	1.54	1.82
Calcite	0.11	0.10	0.28	0.13	0.00	0.00	0.00	0.00	1.72	2.33	0.00	0.00	0.00	0.00	0.00	0.00	0.00	0.00	0.02
Rutile	0.62	0.55	0.59	1.08	0.51	0.47	0.57	0.47	0.47	0.51	0.62	0.95	0.60	0.67	0.58	0.73	0.72	0.76	0.56
Apatite	0.32	0.27	0.31	0.46	0.37	0.35	0.42	0.34	0.29	0.27	0.37	0.46	0.40	0.56	0.38	0.44	0.46	0.46	0.52
Zircon	0.03	0.01	0.01	0.01	0.03	0.03	0.02	0.04	0.04	0.01	0.01	0.01	0.01	0.01	0.02	0.01	0.01	0.02	0.01
Others	0.01	0.03	0.02	0.02	0.16	0.02	0.02	0.02	0.02	0.01	0.01	0.02	0.03	0.04	0.04	0.01	0.01	0.01	0.02
Unclassified	0.70	0.93	0.89	0.88	0.56	0.55	0.62	0.67	0.53	0.68	0.80	0.88	0.87	0.89	1.10	0.83	0.82	0.79	0.95

Id	SK12A	SK12B	SK12C	SK12D	SK12E	SK12F	SK12G	SK13A	SK13B	SK13C	SK13D	SK13E	SK13F	SK13G	SK13H	SK13I	SK13J	SK13K	SK13L	SK14
Bed Type	HB-base	HB	HB	HB-top	HB-base	HB	HB-top	HB-base	HB-top	HB-base	HB	HB-top	TURB-base	TURB-top	HB-base	HB	HB-top	HB-base	HB-top	AMAL-mid
Mineral Mass (%)																				
Quartz	38.62	35.88	36.12	35.27	41.46	36.61	35.96	43.35	34.39	44.40	34.73	36.94	48.16	38.40	31.53	30.94	29.82	45.21	30.74	42.94
Plagioclase	28.71	27.28	29.11	26.11	32.18	30.67	25.40	29.25	24.56	34.18	27.05	29.12	33.05	32.52	29.27	25.67	27.08	34.00	28.18	35.96
K-Feldspar	2.53	2.43	1.96	1.75	1.97	2.01	2.00	1.95	1.58	2.08	1.87	1.57	1.79	2.00	2.21	2.14	1.74	2.00	1.60	1.51
Muscovite	1.50	1.92	2.40	1.78	1.34	1.68	2.00	1.26	1.65	1.12	1.94	1.86	1.17	2.16	1.78	2.10	2.22	1.36	2.25	1.15
Illite	19.61	22.43	20.07	24.58	14.04	19.25	19.96	15.00	28.62	12.45	22.94	20.11	6.90	13.25	28.59	28.08	26.70	8.11	25.06	10.70
Chlorite	5.13	5.09	5.93	6.23	5.39	5.37	5.23	5.63	5.35	5.21	5.67	5.66	4.36	7.22	4.77	5.65	7.40	4.93	7.32	5.26
Other clays	1.60	2.09	1.91	2.06	1.39	2.02	2.38	1.57	1.84	1.84	2.43	2.19	1.26	1.82	1.73	1.97	2.46	1.44	2.09	1.02
Calcite	0.00	0.46	0.23	0.00	0.00	0.00	0.00	0.00	0.00	0.00	0.00	0.00	0.00	0.00	0.00	0.00	0.01	0.38	0.01	0.01
Rutile	0.80	0.85	0.86	0.95	0.88	0.82	0.81	0.75	0.97	0.66	0.87	0.90	0.63	0.68	0.86	0.92	0.97	0.99	1.00	0.64
Apatite	0.47	0.45	0.54	0.55	0.50	0.45	0.48	0.50	0.54	0.47	0.47	0.47	0.34	0.41	0.50	0.50	0.58	0.38	0.56	0.38
Zircon	0.02	0.02	0.02	0.02	0.03	0.02	0.02	0.02	0.02	0.02	0.02	0.02	0.02	0.02	0.02	0.02	0.09	0.03	0.03	0.03
Others	0.14	0.22	0.07	0.14	0.05	0.39	0.46	0.08	0.06	0.08	0.73	0.05	0.27	0.17	0.05	0.16	0.30	0.05	0.33	0.02
Unclassified	0.67	0.89	0.81	0.56	0.76	0.81	1.29	0.73	0.42	0.50	1.27	0.90	1.45	1.25	1.70	0.65	0.80	1.16	0.79	0.44
Mineral Volume (%)																				
Quartz	39.24	36.53	36.74	35.97	42.00	37.23	36.61	43.92	35.12	44.93	35.45	37.56	48.58	38.92	32.19	31.60	30.49	45.62	31.41	43.36
Plagioclase	29.23	27.83	29.66	26.68	32.67	31.15	25.99	29.70	25.13	31.61	27.67	29.67	34.00	33.02	26.86	27.49	27.67	34.73	28.85	36.33
K-Feldspar	2.63	2.53	2.05	1.83	2.04	2.09	2.09	1.93	1.66	2.16	1.96	1.96	1.86	2.08	2.31	2.24	1.83	2.07	1.68	1.56
Muscovite	1.42	1.81	2.27	1.68	1.26	1.59	1.89	1.18	1.57	1.05	1.84	1.76	1.09	2.03	1.69	1.99	2.11	1.27	2.14	1.09
Illite	19.02	21.80	19.49	23.93	13.58	18.69	19.41	14.51	27.90	12.02	22.35	19.52	6.64	12.82	27.85	27.37	26.05	7.81	24.46	10.32
Chlorite	5.16	5.13	5.98	6.29	5.41	5.41	5.27	5.66	5.41	5.22	5.73	5.70	4.36	7.25	4.82	5.72	7.49	4.92	7.41	5.26
Other clays	1.63	1.96	1.77	1.89	1.26	1.88	2.26	1.43	1.68	1.65	2.31	2.01	1.19	1.75	1.58	1.82	2.27	1.32	1.91	0.91
Calcite	0.00	0.45	0.22	0.00	0.00	0.00	0.00	0.00	0.00	0.00	0.00	0.00	0.00	0.00	0.00	0.00	0.01	0.38	0.01	0.01
Rutile	0.50	0.54	0.60	0.62	0.55	0.52	0.51	0.47	0.61	0.41	0.55	0.50	0.39	0.42	0.54	0.58	0.61	0.37	0.63	0.40
Apatite	0.39	0.37	0.43	0.46	0.42	0.36	0.38	0.42	0.45	0.39	0.39	0.39	0.28	0.34	0.42	0.42	0.46	0.32	0.47	0.32
Zircon	0.01	0.01	0.01	0.01	0.02	0.01	0.01	0.01	0.01	0.01	0.01	0.01	0.01	0.01	0.01	0.01	0.05	0.02	0.01	0.01
Others	0.09	0.15	0.05	0.09	0.03	0.25	0.30	0.06	0.04	0.05	0.48	0.04	0.17	0.11	0.03	0.11	0.20	0.03	0.22	0.02
Unclassified	0.66	0.88	0.80	0.55	0.75	0.80	1.29	0.72	0.42	0.49	1.26	0.89	1.42	1.23	1.69	0.64	0.80	1.13	0.78	0.44

Table 1. Mineralogical composition of samples analysed using QEMSCAN. Heavy outlines mark individual beds, which are classified here as hybrid beds (HB), turbidites (TURB) and thick amalgamated sandstone – see text (AMAL), the lowermost and uppermost samples for each bed are marked (-base and -top respectively).

381x259mm (300 x 300 DPI)

Sample name	Bed Type	Grain count	Vectorial mean (M)	Mean vector magnitude (R)	Vectorial concentration (K)	Distribution type (0.05)
2A	TFD	55243	27.10	0.11	0.23	Von Mises
2B	TFD	59868	19.71	0.18	0.36	Von Mises
2C	TFD	59245	1.32	0.09	0.17	Von Mises
2D	TFD	101249	14.04	0.25	0.52	Von Mises
3A	Turbidite	73993	159.35	0.10	0.21	Von Mises
3B	Turbidite	61991	136.56	0.02	0.04	Uniform
3C	Turbidite	146406	9.15	0.29	0.60	Von Mises
3D	Amal. Turbidite	48116	5.69	0.12	0.24	Von Mises
3E	Amal. Turbidite	44879	20.18	0.17	0.34	Von Mises
3F	Amal. Turbidite	56065	26.47	0.07	0.13	Uniform
4A	TFD	33527	22.88	0.16	0.32	Von Mises
4B	TFD	88577	176.47	0.19	0.39	Von Mises
4C	TFD	80043	1.78	0.19	0.39	Von Mises
4D	TFD	35400	8.86	0.34	0.72	Von Mises
4E	TFD	67770	161.69	0.17	0.34	Von Mises
4F	TFD	71208	10.71	0.22	0.45	Von Mises
4G	TFD	113744	175.94	0.22	0.46	Von Mises
4H	TFD	98892	9.45	0.28	0.57	Von Mises
4I	TFD	37427	178.45	0.33	0.69	Von Mises
12A	TFD	43312	1.19	0.25	0.51	Von Mises
12B	TFD	46508	13.38	0.31	0.65	Von Mises
12C	TFD	40441	167.34	0.17	0.35	Von Mises
12D	TFD	8246	7.18	0.35	0.75	Von Mises
12E	TFD	74736	21.73	0.28	0.59	Von Mises
12F	TFD	38182	6.53	0.22	0.45	Von Mises
12G	TFD	56020	176.10	0.12	0.25	Von Mises
13A	TFD	53342	2.39	0.26	0.53	Von Mises
13B	TFD	5934	8.84	0.32	0.68	Von Mises
13C	TFD	32897	10.16	0.23	0.48	Von Mises
13D	TFD	27875	158.87	0.24	0.50	Von Mises
13E	TFD	45056	176.67	0.24	0.48	Von Mises
13F	Turbidite	32994	162.82	0.14	0.27	Von Mises
13G	Turbidite	70501	151.62	0.05	0.10	Uniform
13H	TFD	9710	12.33	0.22	0.45	Von Mises
13I	TFD	28323	176.61	0.27	0.56	Von Mises
13J	TFD	6768	5.96	0.33	0.71	Von Mises
13K	TFD	13707	2.09	0.13	0.27	Uniform
13L	TFD	22479	5.79	0.25	0.53	Von Mises
14A	Amal .Turbidite	59829	175.50	0.19	0.38	Von Mises

Table 2. Grain fabric data. Heavy outlines mark individual beds, which are classified here as HB (hybrid bed), TURB (turbidite) and AMAL (thick amalgamated sandstone – see text).

265x182mm (300 x 300 DPI)